Overcoming Conductivity-Stretchability Tradeoff in Soft Conductive Composites Through Liquid Metal Junctions

Aminur Rahman[a], Mohammad Madadi[a], Jiexian Ma[a], Pu Zhang[a*]

[a] Department of Mechanical Engineering, State University of New York at Binghamton, Binghamton, NY 13902, United States

[*] Email: pzhang@binghamton.edu

ABSTRACT: Soft conductive composites are significant components of soft and wearable electronics. Existing soft conductive composites encounter difficulties in attaining 10% of copper's electrical conductivity whilst maintaining high stretchability. In this work, a novel 'soft conductive junction' concept is introduced to overcome the conductivity-stretchability tradeoff. This new paradigm of soft conductive composites consists of an interwoven copper fiber network embedded in a compliant elastomer matrix. The fiber junctions are connected using liquid metal bridge, which significantly lowers the junction resistance without influencing the stretchability of the fiber network. These hybrid composites uphold ultra-high and strain-insensitive conductivity that is around 60,000 S/cm under 55-75% stretch. Notably, the stretchability of these composites can be further enhanced by 2-5 times via tuning the mesh angles through prestrain, while maintaining high conductivity of 27,000-58,000 S/cm. Potential applications of the composites in stretchable circuitry, wearable interconnects, capacitance tactile sensors, and highly stretchable Joule heaters are presented.

KEYWORDS: soft conductive composite, soft junction, liquid metal, soft electronics, Joule heaters

1. INTRODUCTION

Soft conductive composites are widely used in soft electronics,[1,2] flexible and wearable electronics,[3–5] transparent electrodes,[6–10] smart sensors,[11–13] and soft robotics.[14–16] In practice, soft conductive composites[17–19] desire high electrical conductivity, stretchability or flexibility, strain-insensitivity, and cyclic stability. In recent years, several approaches have evolved to develop high-performance soft conductive composites.[12,20–23] The Ashby chart in **Figure 1d** compares the performance of several major types of soft conductive composites including hard filler,[24] liquid metal (LM),[25] and hybrid solid-liquid filler composites.[26] The hard filler composites usually consist of silver or gold nanomaterials[27,28] as primary conductive networks. Such hard filler composites exhibit excellent initial conductivity but their resistance increases significantly under stretch[24] due to damage, resulting in limited strain-insensitive stretchability. Their overall performance also deteriorates quickly under cyclic stretching or bending.[12,29] To circumvent the rigidity-mismatch issue in hard filler composites, researchers developed liquid filler composites with LMs as the most popular filler for their good conductivity (3-3.5×10^4 S/cm).[30] LM composites have improved strain-insensitive stretchability compared to hard-filler composites but still suffer from bottlenecks such as limited conductivity or strain-sensitive conductivity[11,31,32]. For example, most of the LM composites exhibit strain-insensitive conductivity lower than 10,000 S/cm[32–37]. Although some researchers achieve higher conductivity by increasing the volume ratio of LM, their conductivities are usually strain sensitive[32,38–41]. Overall, there is a conductivity-stretchability tradeoff for soft conductive composites containing only hard or liquid fillers.[19,42] A possible solution is to adopt a hybrid filler approach that combines the advantages of solid and liquid fillers

and achieve both high conductivity and stretchability simultaneously.[43–46] This hybrid filler approach is still an emerging field with new materials being reported. Nevertheless, the existing hybrid filler composites also encounter difficulties in attaining strain-insensitive conductivity[47] targeting 4-6×10^4 S/cm (as compared to copper, 6×10^5 S/cm) whilst maintaining at least 30% stretchability for certain applications in flexible and wearable electronics. This work aims at targeting this limit.

In this work, we propose a novel 'soft conductive junction' concept (**see Figure 1c**) to overcome the conductivity-stretchability tradeoff. This new paradigm of soft conductive composites consists of an interwoven copper fiber network embedded in a compliant elastomer matrix. The fiber junctions are connected using liquid metal bridge (**Figure S6**, and **Figure S16**, Supporting Information), which significantly lowers the junction resistance without influencing the stretchability of the fiber network. This approach offers three key novelties: soft conductive junction, hybrid material architecture, and controllable mechanical stretchability. The designed composites are well suited for applications including stretchable circuitry, wearable interconnects, capacitance tactile sensors, and highly stretchable Joule heaters.

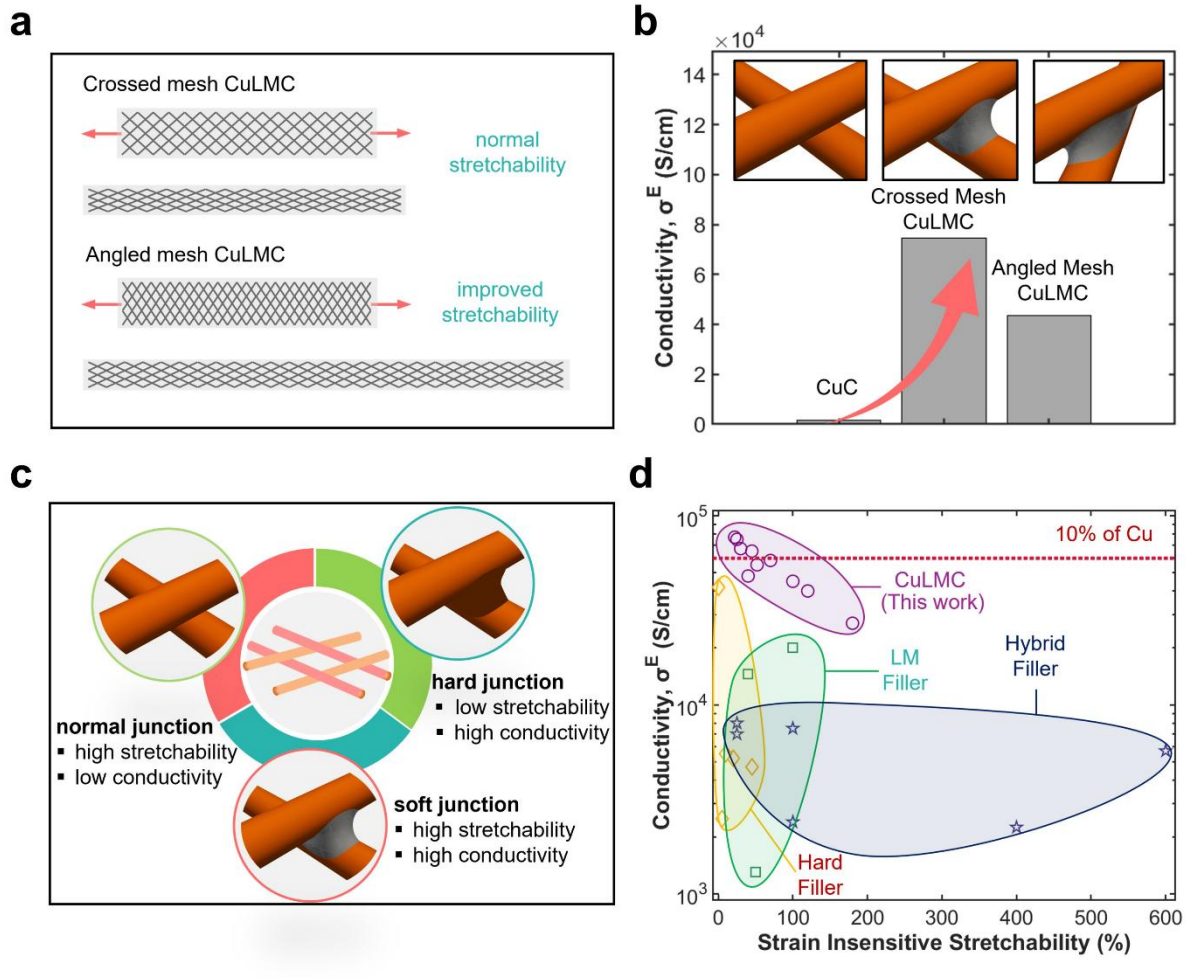

Figure 1. a) The CuLMC consists of a stretchable copper mesh embedded in an elastomer matrix. The stretchability can be enhanced dramatically by using angled mesh (detailed in **Figure S1**, Supporting Information). b) The LM junctions significantly increase electrical conductivity of the composites by reducing junction resistance. Usually, 20-60 fold of conductivity improvement is observed. c) Comparison of the electromechanical characteristics of different junction types: normal, hard, and soft junction. The normal and hard junctions suffer from stretchability-conductivity tradeoff as either low conductivity or low stretchability. The LM-based soft junction overcomes this tradeoff and attains high stretchability and conductivity simultaneously. d) This Ashby chart compares the electrical conductivity and strain-insensitive stretchability of soft conductive composites: hard filler ◊, LM filler □, hybrid filler ☆, CuLMC ○. The CuLMCs exhibit very high conductivity exceeding 10% of Cu. Detailed data are tabulated in **Table S2**, Supporting Information.

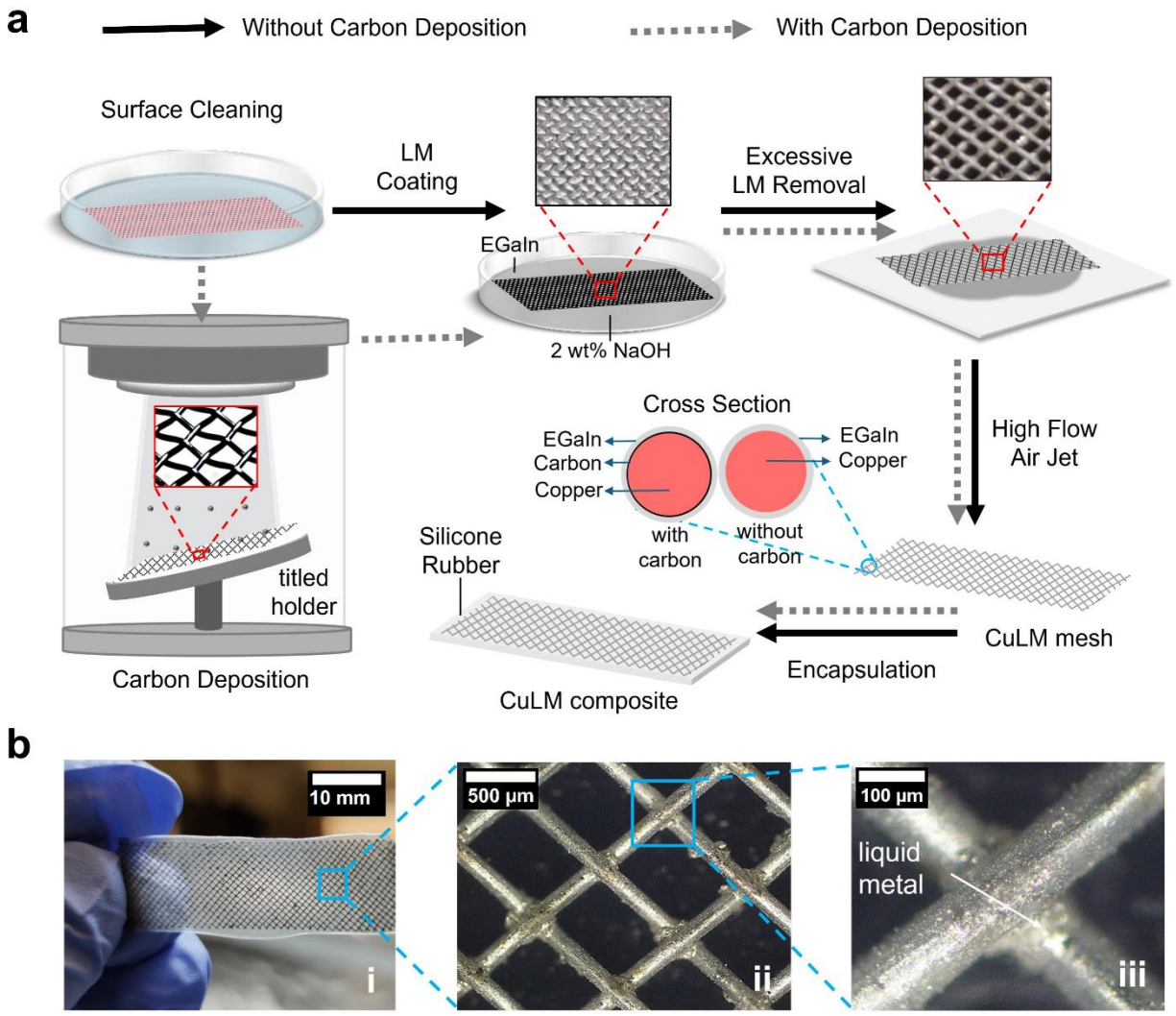

Figure 2. The fabrication process of CuLMCs. Two different approaches are employed: approach 1 without carbon deposition and approach 2 with carbon deposition. a) In approach 1, the process sequentially consists of surface cleaning, LM coating, removal of excessive LM, and PDMS encapsulation. For approach 2, approximately 10 nm of carbon is deposited by thermal evaporation process before the LM coating step. b) Optical microscopy images of fabricated CuLMCs. LM fills in the fiber junctions and forms a soft liquid bridge. There is an ultra-thin layer of LM residual on the fiber as well, which has negligible contributions to the electrical conductivity.

2. OVERVIEW OF DESIGN MECHANISM

Principally, hybrid filler composites utilize the synergy of multiple percolation networks, usually a primary network (e.g., silver nanoflakes or nanowires) with high conductivity and a secondary network (e.g., LM nanodroplets) with high stretchability. The overall conductivity of the composite mainly depends on the microstructure[46] and percolation of the primary network.[48] So the primary network prefers hard metal materials with large aspect ratios, i.e., wires/fibers[49] rather than particles/flakes. [26,43,50] As to the percolation, the contact resistance between hard fillers is a limiting factor[51] for electrical conductivity. Therefore, in order to discover hybrid filler composites with high performance, we need to not only design the microstructure of the primary network but also tackle the contact resistance issue. Considering that we aim to obtain conductivity comparable to 10% of copper, a woven fiber network is an ideal microstructural design for the primary network given its high stretchability and high-volume ratio. In contrast, the well-studied lattice materials usually do not sustain much stretchability.[51,52] As regard to the inter-fiber junctions of a woven fiber network, researchers used to weld them to reduce the high contact resistance,[53–56] i.e. the hard junction approach in **Figure 1c**. An intermetallic bridge[57] approach was also utilized to reduce contact resistance but strain-insensitivity was not achieved due to the rigidity of the junction. Such a hard junction approach inevitably increases the junction rigidity and devastates the stretchability of the network.[56,58,59] To overcome this issue, we propose a LM-based soft junction concept in this work, as shown in **Figure 1c**. For the soft junction approach, the fiber junctions are connected by LM bridges (**Figure S6**, and **Figure S16**, Supporting Information), which are fluidic and conductive. This new approach not only mitigates the contact resistance but also retains the mobility of the fiber junctions and the woven fiber network.

Using this 'soft conductive junction' concept, we introduce a new class of copper-LM composites (CuLMCs) with ultra-high and strain-insensitive conductivity, high stretchability, and excellent cyclic stability. The CuLMCs consist of a woven copper mesh, LM-based soft junctions, and a compliant elastomer matrix. The stretchability of CuLMC is attributed to the mesh geometry (**Figure 1a**) and the conductivity improvement is derived from the LM-based soft junctions. The Ashby chart in **Figure 1d** and **Figure S12** (Supporting Information) compares the electrical conductivity of CuLMCs and state-of-the-art composites in the literature. Most composites exhibit strain-insensitive conductivity in the range of 1,000-20,000 S/cm. The fabricated CuLMCs can provide strain-insensitive conductivity exceeding 10% of copper (up to 77,000 S/cm). Depending on the opening rate and prestrain, it is also capable to provide very high stretchability up to 180%. In some cases, CuLMCs can achieve conductivity around 60,000 S/cm under 45-70% stretch, which are remarkable records for soft conductive composites. **Figure 1b** shows the role of LM junctions on the conductivity improvement for copper mesh composite (CuC) without LM junctions, original CuLMCs, and prestrained CuLMCs. Usually, 20- to 60-fold of conductivity improvement was found by adding LM junctions. Moreover, the overall electrical conductivity and stretchability of CuLMCs can be tailored by tuning the geometric pattern, fiber thickness, opening rate, and prestrain. With such remarkable records of conductivity, stretchability, and tailorability, CuLMCs have promising applications in soft and wearable electronics, not to mention their facile and low-cost manufacturability.

3. EXPERIMENTAL SECTION

3.1 Materials. In this work, four different sizes of copper mesh (20, 30, 40, 60) were used. The mesh sample was cut into small pieces diagonally (45^{o} along the fiber direction) from the bulk

woven mesh (Laohu and Skypro, China). The fiber diameters and opening rates are shown in **Table S1**, Supporting Information. NaOH was acquired from Fisher Scientific. Eutectic gallium-indium (EGaIn, $Ga_{75.5}In_{24.5}$) was obtained by alloying Ga and In metals (RotoMetals Inc.) in an oven. The silicone rubber Ecoflex 00-30 was from Smooth-On.

3.2 Composites without Carbon Coating. To fabricate CuLMCs, copper mesh was sectioned diagonally at a 45^{o} angle relative to the fiber orientation from a larger stock. The surface was rinsed with deionized water for 2 min to remove unwanted impurities from the mesh surface. Afterward, the mesh was dried on a hotplate at 40^{o}C for 2 min. The LM coating bath consists of 2wt.% aqueous NaOH and EGaIn. Initially, the surface tension of LM would prevent it from spreading over the mesh surface and junctions spontaneously. Gentle rubbing was applied until LM spreads all over the surface. Nevertheless, the pores of copper mesh were also filled with LM as depicted in **Figure 2a** (top middle). The excessive LM was then meticulously removed by wiping with filter paper. High-pressure air jet was also applied to ensure proper removal. After removing excessive LM, the mesh pores are clear and LM predominately accumulates near junctions, as shown in **Figure 2b** (bottom right), **Figure S6**, and **Figure S16**, Supporting Information. To manufacture prestrained CuLMCs, the angled mesh (**Figure S1**, Supporting Information) is used. For encapsulation, the LM-coated copper mesh is fixed on a glass slide and Ecoflex 00-30 is spread on the surface followed by vacuum degassing for 5 min (VWR vacuum oven) to remove air bubbles. The assembly was subsequently sandwiched with another glass slide and clamped. The system was cured at 65^{o}C for 4 hours on a hot plate, followed by room temperature curing for 12 hours to obtain the final composite samples. A similar procedure was followed to fabricate brass-LM composites for the Joule heating applications. No carbon coating is applied to the brass mesh.

3.3. Composites with Carbon Coating. In addition, for composites with anti-aging behavior, the copper mesh was deposited with a thin layer of carbon before LM coating. This additional layer of carbon serves as a barrier between Cu and LM, enhancing the durability and functional lifespan of the CuLMCs. Specifically, the cleaned and dried copper mesh is coated with carbon coating (108carbon Cressington Scientific Instruments) under 10^{-4} mbar vacuum pressure. To produce plasma, a 100mA current was supplied for 5 seconds. Approximately 10nm carbon coating was deposited on each side of the copper mesh. In the deposition process, a tilted sample holder was used for better carbon particle distribution on the 3D structure.

3.4. Tensile Testing. Rectangular specimens (60mm × 11mm) were tested on a tensile tester (eXpert 4000, ADMET Inc.) with a 5N load cell. Initial gauge length of 40mm and an extension rate of 0.5mm/sec were used. For each sample, at least three specimens were tested.

3.5. IR Imaging. Thermal images were taken using a pair of FLIR camera (E5 and A310) and processed by FLIR tools software and MATLAB.

3.6. Electromechanical Testing. The electromechanical behavior of the composites was characterized by performing mechanical and electrical testing simultaneously in a synchronized way. A four-wire setup (see **Figure S9a**, Supporting Information) was built to measure the electrical resistance using a Keithley 2110 digital multimeter and Aglient E3612A DC power supply. Two ends of the CuLMC sample were connected to additional wiring using copper tape, and insulated by double-sided tape and adhesive tape. The thickness of each CuLMC specimen was measured using an optical microscope. The electrical conductivity was calculated from the formula $\sigma^E = L/(RWt)$, where L, W, t, R are respectively length, width, thickness, and resistance of the composite specimen.

The bending test was conducted by a setup (**Figure S9b** and **S9c**, Supporting Information) using 3D printed substrates with designed radii for each type of samples. The required radius was calculated from the formula, $\varepsilon_b = (t_{support} + t_{sample})/2r$, where $t_{support}$, t_{sample}, r are respectively thickness of support, sample thickness, and substrate radius. Resistance was measured by a Keithley 2110 digital multimeter. For cyclic testing, a triangular strain profile was used with a 0.5mm/sec extension rate and 15% strain amplitude.

3.7. Fabrication of Interconnects, Capacitive Pressure Sensor, Flexible Heaters and Heat Activated Actuators. LM-coated copper mesh was cut into required shapes (rectangular strip) and connected to the LED using conductive copper paste (843WB, MG Chemicals). The stretchable circuit was obtained by encapsulating the assembly into Ecoflex 00-30.

The capacitive pressure sensor was designed as a sandwich structure, using polyurethane foam (500μm thick) embedded between two CuLMC layers on top and bottom. A slicer (SliceMaster, Jasco Inc.) was used to slice the polyurethane foam at the required thickness. All the layers were bonded together with adhesive. The rectangular sensor (10mm × 10mm) was tested for various compression modes, such as tapping, pressure variance, and object grabbing. The data was recorded as a function of capacitance using the Keithley 2110 digital multimeter.

The mesh 30 brass-LM (conductivity is 14166 S/cm, which is approximately 10% of pure Brass) composite strip was precisely tailored into narrow dimensions (80mm × 8mm) to enable conformal attachment onto curved surfaces, including human knee and cylindrical substrates. For the transparency heat actuator, a brass-LM composite formed the structural core, encapsulated within a PDMS/Paraffin Wax (PW) matrix. To achieve thermally induced bending actuation, the entire assembly was mechanically stretched, and a thin PW layer was uniformly deposited onto the

composite. Upon solidification of the PW, the actuator was further encapsulated within an additional PDMS layer to ensure structural integrity and responsive performance.

4. RESULTS AND DISCUSSIONS

4.1. Microstructures. The fabrication process of CuLMCs is illustrated in **Figure 2a** and introduced in the section 3. As shown in **Figure 2b**, **Figure S16** (Supporting Information), LM in CuLMCs predominantly gathers near the fiber junctions, serving as a conductive liquid bridge to reduce the contact resistance. In **Figure 2b**, LM clearly forms a meniscus in the junctions and shows excellent wetting condition with the copper fibers. Such a good wetting condition is partially attributed to the $CuGa_2$ intermetallic formed at the interfaces. If other metal mesh is employed, the wetting condition will vary, and LM junctions may not form properly. Our preliminary results indicate that stainless steel mesh does not wet well with LM. From **Figure 2b**, there is an ultrathin layer of LM surrounding the fibers as residuals from the LM coating process. This residual layer has negligible influence on the electrical conductivity of the composite. The CuLMC is highly stretchable because of the unique geometric feature of the woven mesh. Under uniaxial stretch, the fibers can rotate freely to accommodate the longitudinal strain. The advantage of this soft junction concept is that LM in the junction allows the fibers to rotate freely, as opposed to a hard junction that constrains the fiber rotation. When the deformation is released, the junction recovers to its original shape with the LM bridge flowing back meanwhile. The morphology of the LM bridge is discussed in **Figure S6e**, Supporting Information. Note that the soft silicone matrix plays an indispensable role on the functionality as it helps to confine LM in the junction without compromising electrical conductance (**Figure S6d**, Supporting Information), which shows stable

electromechanical performance under cyclic loadings. In the fabrication process, the copper mesh is sandwiched between two glass slides. Therefore, the thickness of the composite film is twice of the fiber diameter. For composites with different mesh sizes, we have recorded a thickness of 160μm, 200μm, 220μm, and 300μm, respectively, for mesh 60, 40, 30, and 20 CuLMCs. In practice, thicker samples can be prepared by laminating multiple layers of metal mesh together.

4.2. Mechanical and Electromechanical Behaviors. The mechanical behaviors of the CuLMCs are characterized and compared to that of the copper mesh composites (CuCs), i.e., the ones without LM junctions. Experimental data (**Figures S7a** and **S7c**, Supporting Information) show that the stress-strain behavior of the composites with (CuLMCs) and without (CuCs) LM junctions are nearly identical, implying that the LM junctions do not have noticeable impact on mechanical performance. Overall, the composites behave like a hyperelastic material, similar to the Ecoflex 00-30 matrix. Mechanically, the composites undergo three different stages under uniaxial loading, as fiber rotation, fiber interlocking, and fiber pullout failure (**Figure S7a** and **S7c**, Supporting Information). Regarding the stress-strain curves, the interlocking stage starts with rapid increase of stress and ends at the peak stress where fiber pullout occurs. From the application perspective, the composites should usually be operated in the fiber rotation stage to mitigate damage.

The stretchability of CuLMCs mainly depends on their mesh sizes, or more precisely, the opening rate. Each mesh size has a different opening rate (**Table S1**, Supporting Information), a parameter indicating how dense the fibers are (**Figure 3f**, top row). For a higher opening rate, the fibers can rotate more freely before interlocking, which leads to higher stretchability of the composite. This relation is illustrated in **Figure 3b**, where the mesh 20 one has the highest opening rate and thus the stretchability. The stretchability relation in **Figure 3b** is also confirmed by the

stress-strain curves in **Figure 3d** for CuLMCs with different mesh sizes. Typical microstructures before and after stretching are compared in **Figure 3f** as well.

The LM junctions completely change the electrical properties of the CuLMCs. The high junction resistance of copper mesh leads to poor electrical conductivity, but the LM junctions effectively mitigate the junction resistance (**Table S5**, Supporting Information) and boost the conductivity. As depicted in **Figure 3a** (and **Figure S5b**, Supporting Information), our data show that the LM junctions increase the conductivity by 20- to 60-fold. More specifically, the highest and lowest conductivity is observed for mesh 60 composite (77,000S/cm) and mesh 20 composite (45,000S/cm), respectively. By comparing to the conductivity of pure copper (596,000S/cm),[60] CuLMCs can readily surpass 10% of Cu's conductivity, a value hard to reach for soft conductors. The electrical conductivity is also correlated to the opening rate of the mesh (see **Figure 3c**) as a higher opening rate leads to lower conductivity. Note that the conductivity is mostly dominated by the LM junctions, not the residual LM coating covered on the mesh (**Figure S6c**, Supporting Information)

Besides the high conductivity and stretchability, another prominent feature of CuLMCs is their strain-insensitive conductivity (or resistance). The conductivity-strain relations are tested and depicted in **Figure 3e**. In the fiber rotation stage (**Figure S1a-b** and **Figure S6a**, Supporting Information) the electrical conductivity is almost constant under stretch (also in **Figure S6c**, Supporting Information), which is very useful for soft electronics applications. A sudden decline of conductivity usually occurs in the fiber pullout failure stage (close to peak stress), because of the microstructural damage in the composite. The strain-insensitive conductivity is mainly due to the unique geometric characteristic of the CuLMCs. Firstly, although the mesh geometry is distorted under stretch, the percolation network (**Figure S6a** and **Figure S6c**, Supporting

Information) remains the same so the resistance does not change. Secondly, the LM junction has mitigated the contact resistance (**Figure S6b, Figure S16** and **Figure S6e**, Supporting Information) and maintained perfect connections between fibers. Note that the LM's role is indispensable as the conductivity of CuC is very sensitive to strain (**Figure S7b**, Supporting Information). Additionally, the Young's moduli of the CuLMCs are between 0.42 to 0.73 MPa, and are 0.12 to 0.65 MPa for prestrained CuLMCs.

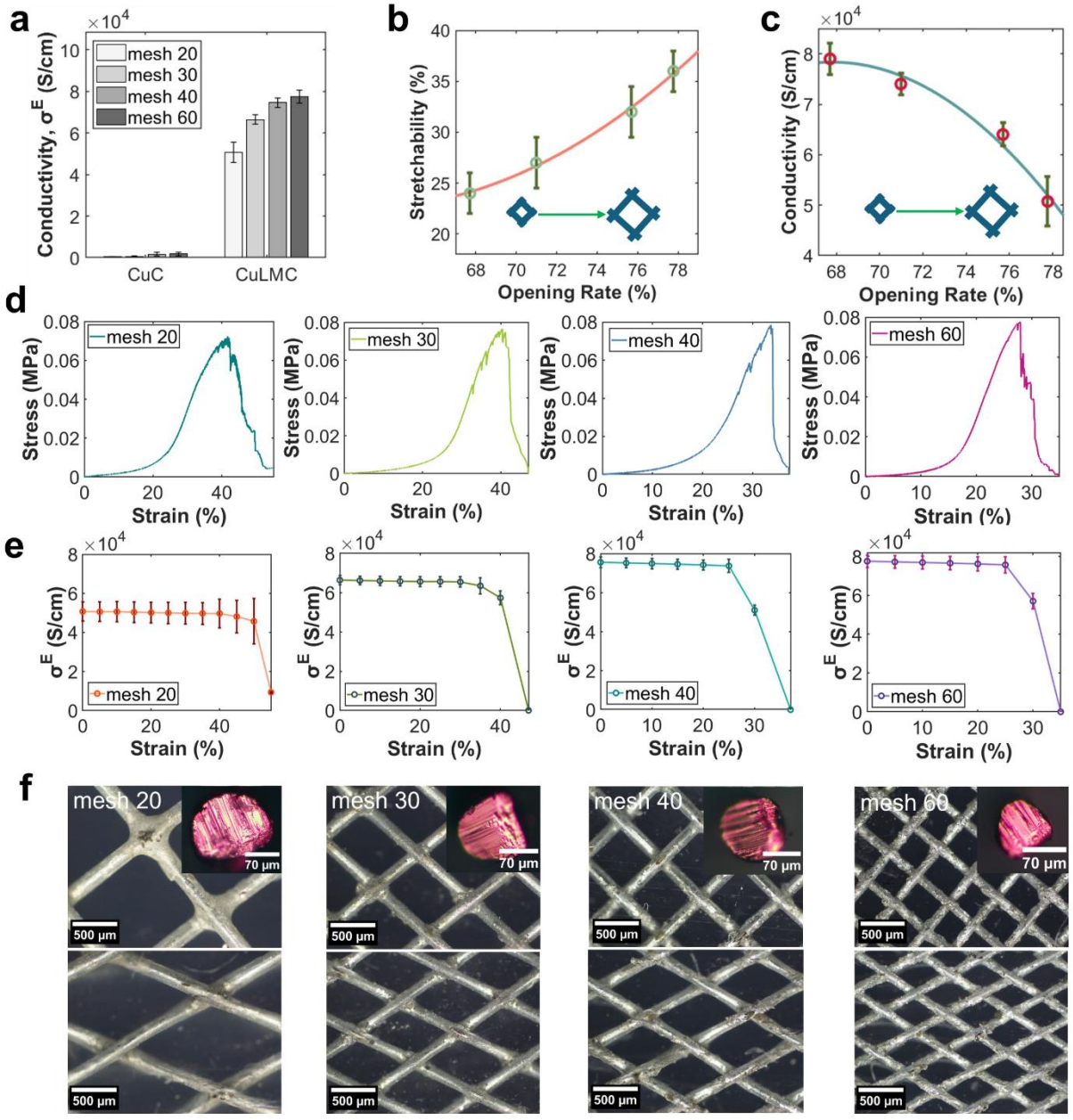

Figure 3. Electromechanical performance of CuCs and CuLMCs. a) CuLMCs demonstrate 20- to 60-fold conductivity increase compared to CuCs, owning to the LM junctions. b) Relationship between stretchability and opening rate of CuLMCs. c) Relationship between conductivity and opening rate. d) Mechanical behavior of CuLMCs with different mesh sizes. e) Electrical conductivity of CuLMCs under stretch for different mesh sizes. f) Optical microscopy images of CuLMCs. Typical cross-sectional profiles of individual fibers are on the top right corners. Both the original state (top row) and stretched state (bottom row, 32% strain for mesh 20, 25% for mesh 30, 24% for mesh 40, and 20% for mesh 60) are presented.

4.3. Enhance Stretchability using Angled Mesh. The stretchability of the CuLMCs can be improved by using angled mesh, i.e., applying prestrain to adjust the intersectional angle of the mesh before encapsulation. The mechanism is easy to understand (**Figure S1**, **Figure S3**, and **Figure S18**, Supporting Information). Due to the geometric feature of the copper mesh, a pre-compressed mesh (**Figure 4a**) exhibits increased stretchability compared to the original one, with some sacrifice of the electrical conductivity due to the dimension change. For example, we are able to increase the maximum strain of a mesh 40 CuLMC from 25% to 100% by applying a -33% prestrain to the mesh before encapsulation. Hence, by employing prestrain, we can obtain composites with unprecedented conductivity and stretchability simultaneously, which is highly desirable for soft electronics applications. The relations between prestrain, conductivity, and stretchability of the CuLMCs with prestrain can be derived analytically from the geometric relations (**Equations S3** to **S6**, Supporting Information). **Figures 4b** and **4c** present the influence of prestrain on the conductivity and stretchability for CuLMCs with mesh 40. The theoretical solution agrees very well with experimental data. Generally, the stretchability enhancement will sacrifice conductivity to some extent. For example, a -33% prestrain would increase the stretchability by 4-fold (**Figure 4c**) but reduce the conductivity by a half (**Figure 4b**). Such general trends apply for other mesh sizes as well (**Figures S3** and **S6**, Supporting Information). In some cases, we are able to achieve above 150% stretchability for mesh 20 (**Figures S4** and **S8**, Supporting Information). In short, CuLMCs can be precisely tailored through prestrain to meet desired levels of conductivity and stretchability for soft electronic devices, and the theoretical formulae (**Equation S4** and **S6**, Supporting Information) can provide guidance for such design.

To examine the electromechanical performance of the CuLMCs with prestrain, four different types of composite samples with prestrain 0% (i.e., no prestrain), -10%, -20%, and -33% were fabricated using mesh 40 and tested under uniaxial loading. Electromechanical tests (**Figure 4d**, **4e**) suggest that prestrained CuLMCs have similar hyperelastic responses and strain-insensitive conductivity compared to the original one in **Figure 3**. For example, -20% prestrain would result in a conductivity of 58,000 S/cm, close to 10% of pure copper, with a stretchability of 55%. Similar performance was also found for other CuLMCs as listed in **Table S2**, Supporting Information. Such excellent properties are well suited for applications as flexible interconnects.

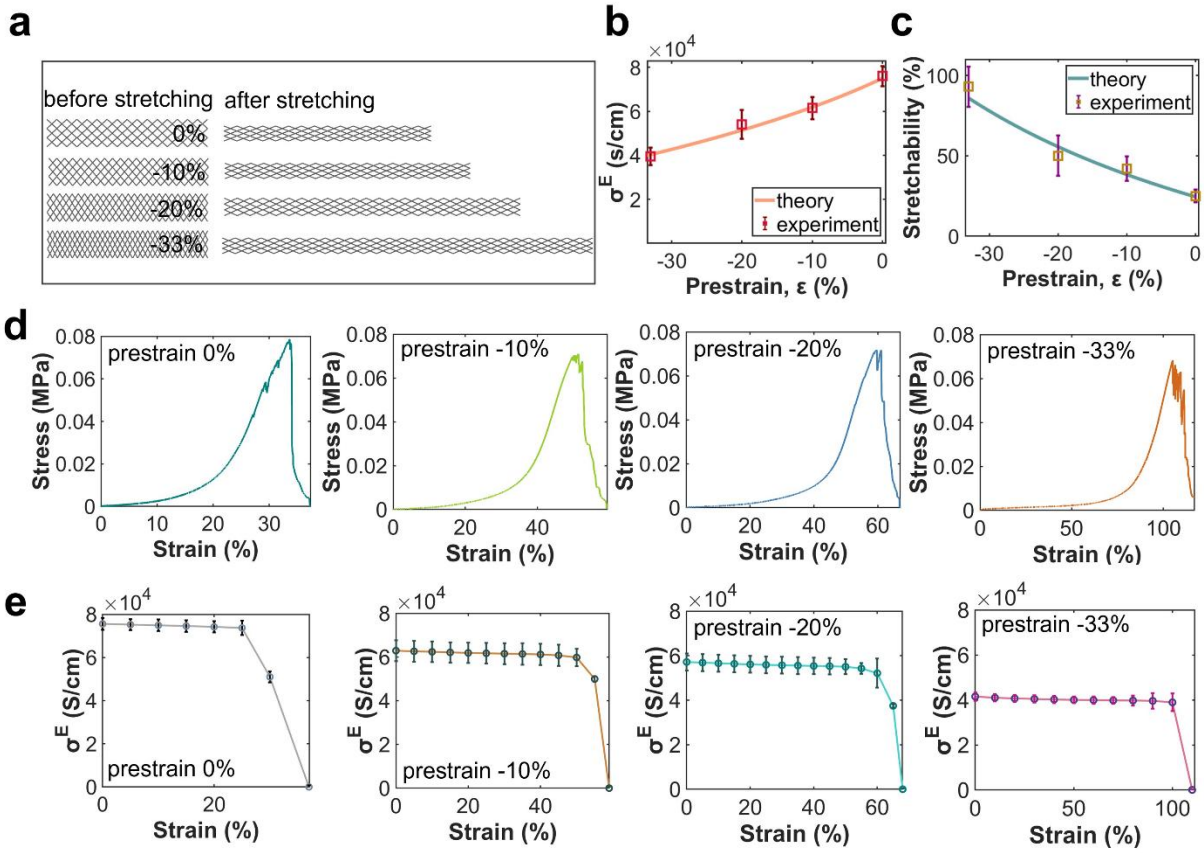

Figure 4. Electromechanical performance of CuLMCs embedded with angled (or prestrained) copper mesh to enhance their stretchability. All data are for mesh size #40 only. The stretchability of the composite can be improved significantly by applying prestrain to the mesh, albeit sacrificing the conductivity to some

extent. a) The pre-compressed mesh has increased stretchability compared to the original one due to the microstructural change. The stretchability of the composite increases from 20% to 100% by applying -33% of prestrain to the mesh. Schematic of stretchability enhancement of CuLMCs. b) Electrical conductivity of CuLMCs under different prestrain level. c) Stretchability of CuLMCs under different prestrain level. d) Stress-strain behaviors of CuLMCs with 0%, -10%, -20%, and -33% prestrain. e) Conductivity-strain behaviors of CuLMCs with different prestrain. The conductivity is overall strain-insensitive until failure occurs.

4.4. Bending Performance. The CuLMCs have remarkable electrical performance under bending deformation, which is also a prominent indicator of flexible electronics. As the CuLMC film is very thin, a supporting polymer layer (polylactic acid sheet, thickness 110μm) is used to obtain uniform tensile bending mode.[61] As shown in **Figure 5a**, this bi-layer design has a substrate radius *r* in a range of 3.4-41 mm. As each mesh size has a different film thickness, the relation between the bending strain and substrate radius is shown in **Figure 5b**. It is observed that for the same substrate radius, a thicker film (e.g., mesh 20) produces greater bending strain compared to the thinner one (e.g., 60 mesh). The bending performance of CuLMCs is characterized by the normalized resistance R/R_0 (herein R_0 and R are resistance before and after bending) versus the bending strain. As shown in **Figure 5c-f**, the normalized resistance R/R_0 remains stable in a wide range of bending strain and only varied by a marginal factor of 2-4%. Even at 4% bending strain (i.e., r = 4-5 mm), these composites show promisingly strain-insensitive resistance, which is around 1.44-1.50mΩ/sq. The normalized resistance of mesh 20 CuLMC (**Figure 5c**) has a slightly larger variance compared to others due to its low opening rate and larger thickness. Considering the flexible electronics applications, conductive composites should have a bending radius of 1-5 mm[62] with an electrical performance degradation of less than 10%.[63] The bending test results of the CuLMCs show stable electrical responses (with 2-4% variation) even at a bending radius of 4-

5 mm. Therefore, CuLMC has the potential in the application of flexible electronics like wearable interconnectors and flexible devices with stable conductivity.

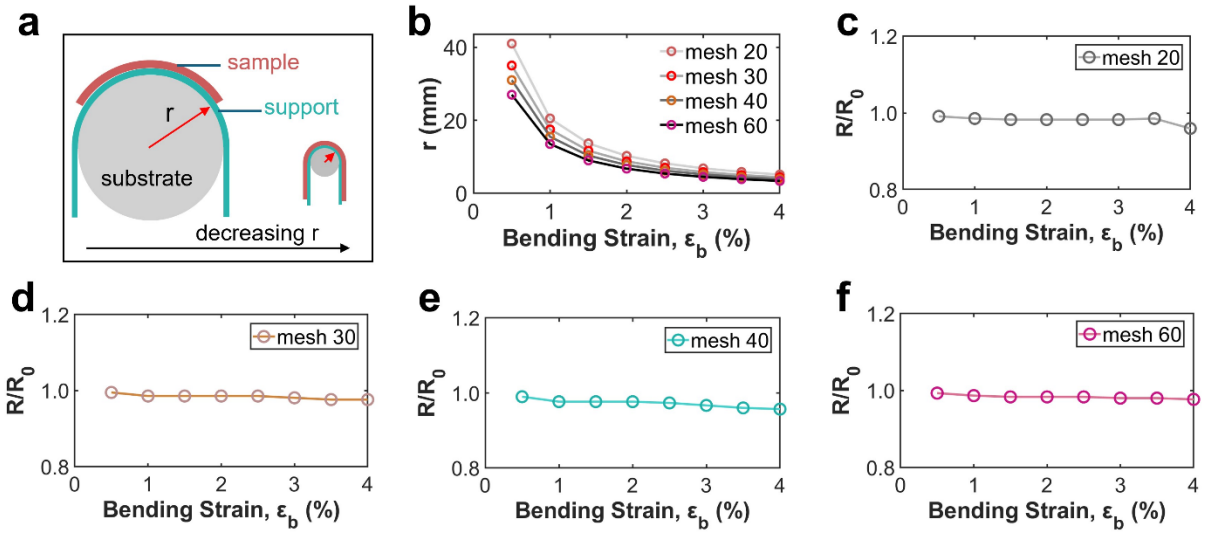

Figure 5. Electromechanical behavior of CuLMCs under bending deformation. a) Illustration of the test setup and bending radius of the substrate. CuLMC is mounted on a flexible support and then bent on a substrate with specific radius. b) The relationship between bending strain and substrate radius for each CuLMC. c-f) Normalized resistance versus bending strain of CuLMCs for different mesh sizes.

4.5. Cyclic Performance and Anti-aging Coating. The cyclic performance of CuLMCs is critical for their applications in soft electronics. We found that the corrosive reaction[64] between Cu and LM has a significant impact on the cyclic performance of CuLMCs, and discovered that a carbon coating on the copper mesh would resolve this problem.

As shown in **Figure 6**, we have recorded resistance changes when the composites experienced cyclic stretch (triangular strain profile, 0 to 15%) for 1000 cycles. Firstly, we examined the influence of Cu-LM reaction on the cyclic performance of CuLMCs (without carbon coating). We conducted cyclic testing for two samples on day 1 (**Figure 6a**) and day 14 (**Figure 6b**) after

fabrication to examine the aging effect. On day 1, optical microscopy images in **Figure 6a** show no sign of corrosive reaction and the junction region contains sufficient LM with a bright metallic color. The cyclic resistance response is also very stable on day 1. After 1000 cycles, normalized resistance R/R_0 changed in the range of 1.004 to 1.014, about 1% fluctuation. In contrast, the aging or corrosion process has a significant impact on the cyclic performance after 14 days. In **Figure 6b**, the optical microscopy images show that the fiber surface becomes dark and LM disappears at junctions, evidencing corrosive reactions between Cu and LM and the formation of intermetallic compound $CuGa_2$.[65] Meanwhile, the cyclic resistance response in **Figure 6b** is unstable given that the normalized resistance changes significantly after just 100 cycles.

To suppress the corrosion process, we deposited a thin carbon coating on the copper mesh before LM coating, as illustrated in **Figure 2**. The detailed composition of carbon coating is evaluated by EDS in **Figure S17**, Supporting Information. Such a thin carbon coating serves as a barrier between Cu and LM to suppress corrosion [66] and preserve the LM junction. We choose carbon coating also because that it is highly conductive and would not impair the electrical conductivity of the composite. Certainly, other noble metal deposition may work as well if the wetting condition is good. **Figure 6c** shows the cyclic performance of a CuLMC sample (with carbon coating) after 14 days of fabrication. By comparing **Figure 6a** and **6c**, the composites with carbon coating showed a negligible aging effect after 14 days. The normalized resistance of the composite in **Figure 6c** is very stable and fluctuates within a 1% range. Besides the stable cyclic resistance performance, optical microscopy images in **Figure 6c** confirm that the corrosive reaction between Cu and LM is unnoticeable and sufficient LM exists in the junctions and surfaces after 14 days. Hence, we conclude that a barrier coating such as a thin carbon layer on the copper mesh is necessary to guarantee the cyclic performance of CuLMCs.

We also tested the stress-strain responses of the CuLMCs under cyclic loading. The CuLMCs exhibit some extent of viscoelastic behaviors, given that there is a hysteresis effect during cyclic loading (**Figure S10a**, Supporting Information). Such a viscoelastic behavior potentially arises from the fiber-fiber friction and intrinsic viscoelastic nature of the Ecoflex 00-30 matrix.[67] Oxidation of the LM phase may contribute to the viscoelastic behaviors as well but the influence may be marginal. In contrast to the viscoelastic behavior, no hysteresis was observed for the cyclic conductivity-strain responses (see **Figure S10b**, Supporting Information).

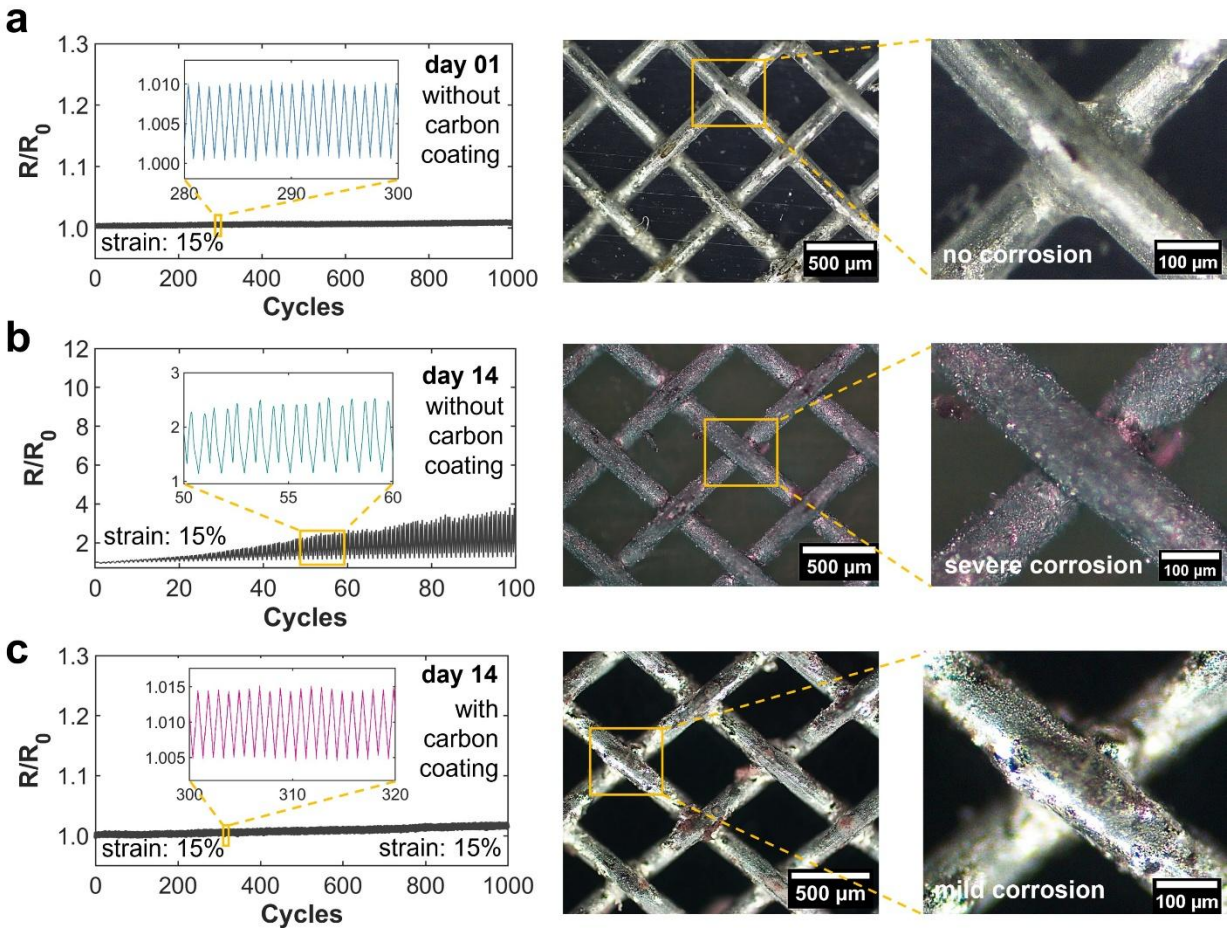

Figure 6. Cyclic electromechanical behavior of mesh 40 CuLMCs. a) Even without carbon coating, the as-fabricated composite has good cyclic performance with stable normalized resistance R/R_o. The OM images indicate the presence of sufficient LM in the junction. b) After 14 days of aging, the composite without

carbon coating shows deteriorated performance under cyclic stretch. Optical microscopy images indicate that the Cu surface becomes darker and the LM junction disappears. This is due to the corrosive reaction between LM and Cu. Consequently, the cyclic testing data shows a large deviation of R/R_o. c) Adding carbon coating on the copper mesh significantly suppresses the aging process and enhances the cyclic stability of the composite. The optical microscopy images show the presence of LM on the surface and junctions after 14 days. The aging process can be suppressed further by depositing thicker carbon coatings.

4.6. Strain-Insensitive Joule Heating Behavior. The strain-insensitive conductivity behavior of the proposed mesh composite with LM junctions is ideal to be employed as highly stretchable and strain-insensitive Joule heaters. For this application, we replace the Cu mesh with a brass mesh as the latter is more suited for Joule heating purposes for its higher Joule heating rate. The Joule heating behaviors of the brass mesh composites are presented in **Figure 7**. In **Figure 7a-b**, we compare the Joule heating performance of brass mesh composites before and after adding LM junctions, which are shown in **Figure 7a** and **7b**, respectively. The thermal images in **Figure 7a-b** indicate that LM junctions remarkably improve the heating uniformity. **Figure 7a-b** also show that brass mesh composite with LM junctions reach higher and more consistent surface temperatures, owning to reduced contact resistance between fibers. The Joule heating performance and power consumption are compared and presented in **Figure S15**, Supporting Information.

Figure **7c-d** show the influence of mechanical strain (0%, 15%, and 30%) and LM junctions on the temperature evolution of the brass mesh composites at fixed voltages (1.0V or 0.8V). Herein, **Figure 7c** and **7d** show results of the samples without and with LM junctions, respectively. From **Figure 7d**, we observe that LM junctions enable the composite Joule heaters with strain-insensitive Joule heating behavior under stretching, which cannot be achieved without the LM junctions (**Figure 7c**). Furthermore, **Figure 7e** shows the strain-insensitive Joule heating behavior of the brass-LM composites with LM junctions under various deformation modes such as

stretching, bending, and twisting without influencing average surface temperatures. The Ashby chart (**Figure 7f**) compares normalized surface temperature ($\Delta T/T_0$) with present literature and evidently shows that the proposed brass-LM composites have the highest stretchability (140% strain) with strain-insensitive Joule heating performance. The angled mesh brass-LM heater shows very high stretchability (**Figure S13**, Supporting Information) with uniform heat distribution and marginal temperature drift under stretching. In addition, the heater exhibited excellent environmental stability, maintaining consistent performance over 20 days **(Figure S14**, Supporting Information). Furthermore, it demonstrated robust cyclic heating reliability with negligible degradation observed across repeated thermal actuation cycles (**Figure S14e**, Supporting Information).

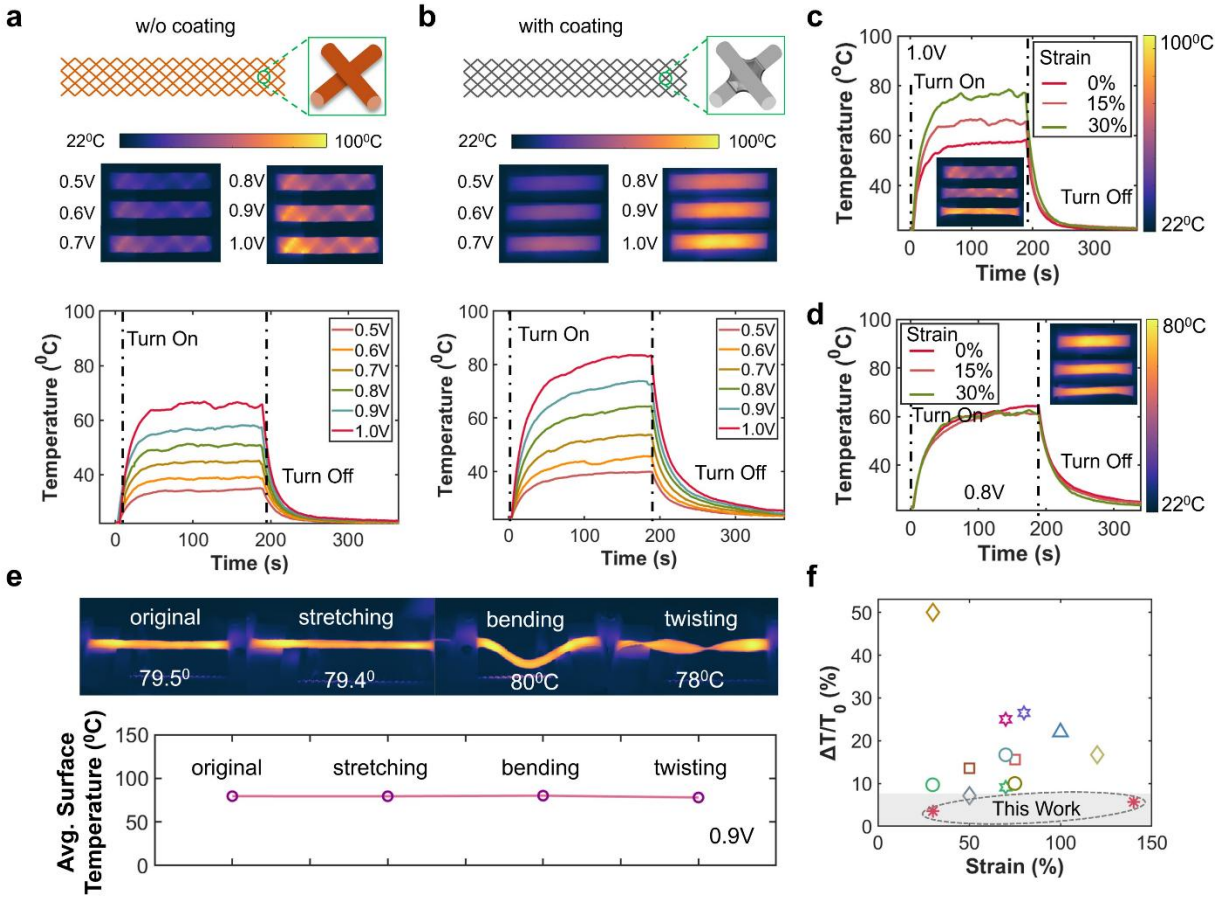

Figure 7. Strain-insensitive joule heating performance of brass mesh composites with LM junctions. a) Brass 30 mesh composites without LM junctions exhibit poor inter-fiber conductivity, localized heating, and thermal inconsistency. b) Brass 30 mesh composites with LM junctions (brass-LM composites) exhibit improved conductivity with more uniform and efficient heating performance. c) Temperature evolution profile of brass mesh composite without LM junctions under stretching. d) Temperature evolution profile of brass mesh composite with LM junctions under stretching. e) Average surface temperature of brass mesh composite with LM junctions under various deformation modes. Strain-insensitive Joule heating performance is observed. f) The Ashby chart shows that the strain-insensitive Joule heating behavior of the proposed brass-LM composites outperforms others with low thermal drift under large strain. Detailed data are tabulated in **Table S7**, Supporting Information.

4.7. Stretchable and Wearable Circuits. To empirically validate the performance, we have implemented CuLMC in a stretchable circuit (**Figure 8a**). In this setup, narrow strips of CuLMC

are connected to LEDs, designed to withstand a variety of mechanical deformation modes. When a voltage is applied, the assembly endures 50% stretching, about 90^0 twisting, and significant twisting/bending. Remarkably, throughout this rigorous process, the LEDs maintain their initial luminosity consistently. The resilience under mechanical stress, combined with electrical performance, potentially unleashes the application in wearable electronics and soft robotics as well. To investigate the compatibility with wearable electronics, CuLMC was integrated with multiple flat LEDs. As an attempt for complex shapes, integrated LEDs with CuLMC strips are connected as a BU-shaped structure. Later, the whole system is transferred and attached to a textile clothing surface. Normally, textile clothing withstands multi-directional deformation. To mimic real-world wearability, various deformation is also applied (**Figure 8b**). The vertical and diagonal elongation on clothing shows that the illumination of LEDs remains stable, which is a potential indication of better circuit functionality and integrity. Exceptional conditions mimicry (**Figure S11**, Supporting Information) such as simultaneous multi-directional bending, rolling, and bending-stretching also exhibited plausibly strain-insensitive conductivity. In the realm of wearable electronics, strain insensitivity is highly suitable for dynamic display and health monitoring devices, where maintaining functionality under stress conditions is decisive.

4.8. Capacitive Pressure Sensor. Pressure or tactile sensors are useful elements for wearable and flexible electronics, soft electronics, virtual reality, etc. As CuLMCs are strain-insensitive, highly conductive, flexible, and stretchable, they would be a good candidate for the capacitive pressure sensor. We have fabricated a capacitive pressure sensor as a sandwich structure by embedding a polyurethane foam layer in the middle and CuLMCs as top-bottom electrodes. The middle layer functions as a diaphragm keeping a certain distance between the electrodes. The actuation mode works based on the parallel distance and surface area of CuLMC electrodes. As

shown in **Figure 8c**, when pressure is applied, the thickness of the middle layer decreases and induces a higher capacitance value. To measure the effectiveness of the actuation principle, various modes of tactile feedback are tested, for instance, normal touch (**Figure 8d**), and haptic touch (**Figure 8f**). For normal touch, it changes the distance and hence the capacitance value, which is reflected by the relative change of capacitance ($\Delta C/C_0$). To check the maximum sensitivity range (**Figure 8e**), the sensor undergoes maximum compression, where it shows approximately 2.5 times shift in sensitivity than the initial value, which means the sensor has a very high sensitivity range. As CuLMCs are flexible, the sensor is capable of detecting haptic touch (**Figure 8f**) such as soft, medium, and hard, which would be potentially useful for designing adaptive robotic hands and smart grippers. To check the viability, another interesting prospect is demonstrated by grabbing a coffee cup (**Figure 8g**). In this case, the sensor was mounted on the palm of the right hand, and in situ capacitance data was then recorded before and after grabbing the object. As the hand palm folded, the sensor triggered the capacitance response and resulted in an abrupt rise in the graph.

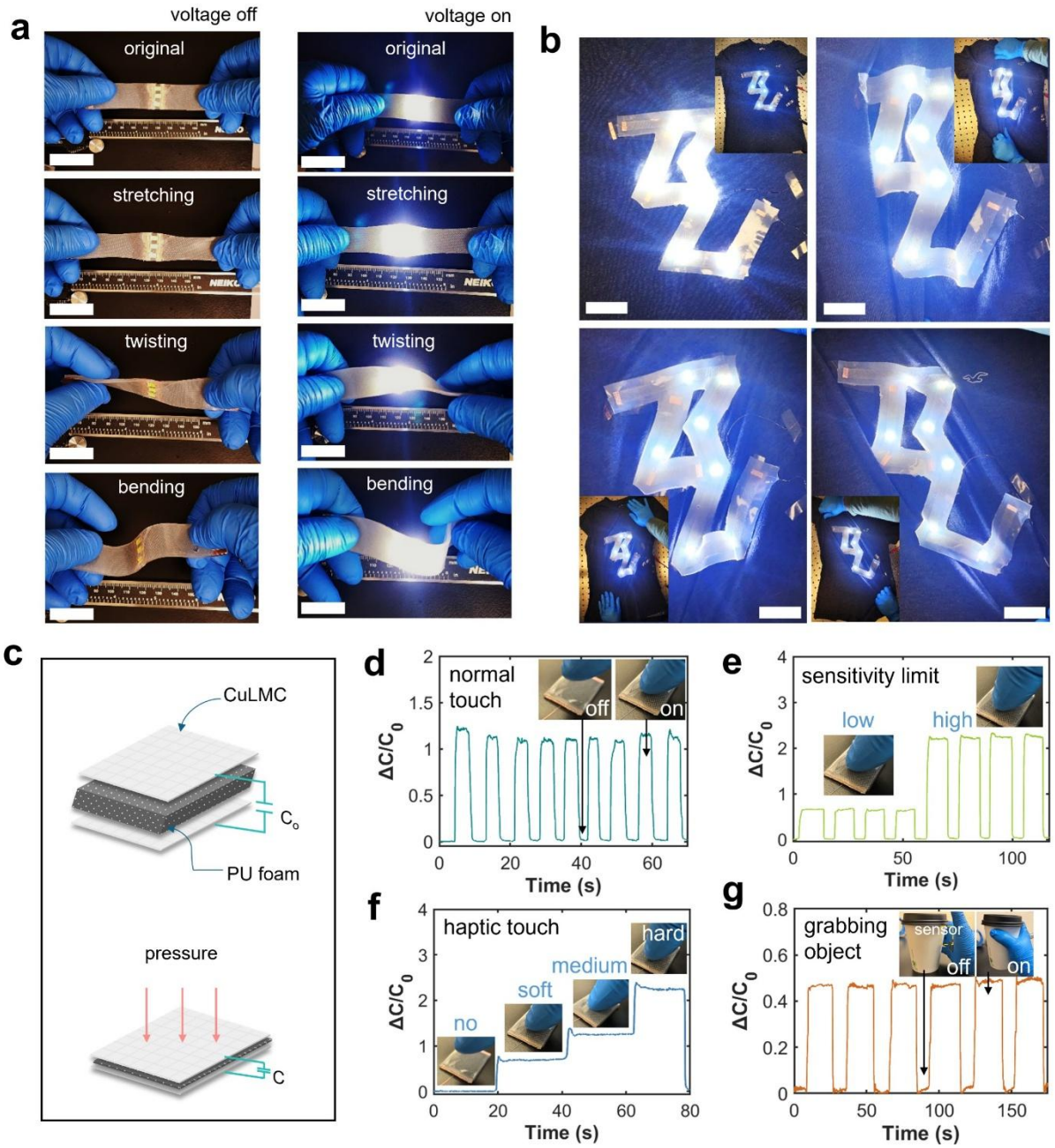

Figure 8. Application of CuLMCs as circuits, wearable interconnects, and pressure/tactile sensors. a) The stretchable circuit is incorporated with surface-mount LEDs backed by CuLMC. CuLMC can endure mechanical deformation in various modes such as stretching, bending, and twisting without compromising the brightness of LEDs. Scale bar 3cm. b) BU-shaped wearable interconnects attached to a textile garment. The interconnect is stretched in vertical and diagonal directions. Scale bar 3cm. c) Schematic of capacitive pressure sensor fabricated as a sandwich structure. d) Normal touch response on the sensor leads to variations in relative capacitance ($\Delta C/C_o$). e) Sensitivity limit measurement by compression. f) Capacitance

responses in different levels of touch (haptic mode). g) Pressure response before and after grabbing an object. The sensor is attached to the hand palm.

4.9. Stretchable Heater, Heat Activated Transparency and Thermo Responsive Bending. Reliable thermal uniformity and strain-insensitive Joule heating performance are desired for flexible and wearable Joule heaters. **Figure 9** illustrates the Joule heating performance of flexible heaters and actuators. A strip of brass-LM composite heater is attached to a human knee (**Figure 9a**) to demonstrate thermotherapy application. It demonstrates mechanical robustness with stable temperature output (50.3°C straight and 49.6°C stretched). The soft Joule heater can also be wrapped around cylindrical and curved surfaces like a vial or pipe. In addition, such a soft Joule heater can also be used for thermal actuation as presented in **Figure 9b-c**. Herein, a switchable transparency actuator is fabricated with a brass-LM composite film as the heating source. PDMS and PW are used to encapsulate the brass-LM film. The actuator is opaque at room temperature but quickly turns transparent when voltage heats it above PW's melting point, revealing the text behind it. Thermo-responsive bending actuation (**Figure 9c**) is achieved using a thin solidified PW layer (300μm). It keeps the actuator flat initially when the voltage is off and bends progressively as the voltage heats PW from solid to liquid phase.

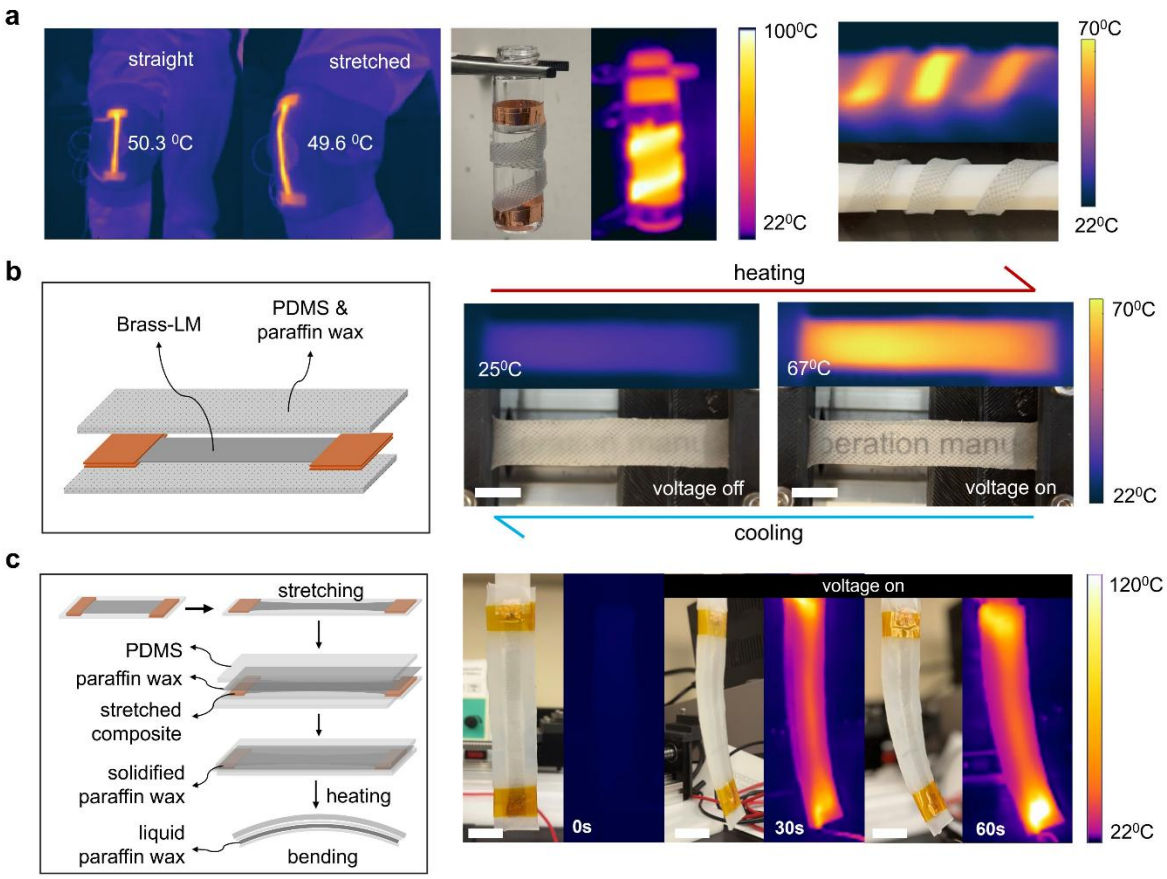

Figure 9. Applications of the brass-LM composites as highly stretchable and strain-insensitive Joule heaters. a) Surface adaptability of flexible heaters for thermotherapy (left) and wrapping heaters (middle and right). b) Schematic and performance of a heat-activated switchable transparency actuator. c) Schematic and demonstration of heat-based bending actuation.

5. CONCLUSION

In this work, we propose a new design concept for soft conductive composites to achieve high conductivity and stretchability simultaneously. It is well known that soft conductors usually suffer from a conductivity-stretchability tradeoff as these two properties usually oppose each other. By examining existing soft conductive composites, we conclude that soft composites with hybrid solid-liquid fillers are the most promising approach to overcome this tradeoff and attain high performance. In order to achieve both high conductivity and stretchability, the hybrid composites

need to have a primary solid network offering conductivity and a secondary liquid network offering stretchability. Employing this concept, we proposed a new class of soft conductive composites named CuLMCs, which consist of a woven copper fiber network, LM-based soft junctions, and a compliant elastomer matrix. The copper fiber network serves as the primary network, highly conductive and stretchable. Meanwhile, the LM junctions mitigate the contact resistance at fiber junctions without influencing their mobility and stretchability. Both the microstructural design and contract resistance treatment are needed to achieve high performance. This 'soft conductive junction' concept shows advantages over the contemporary hard junction approach in terms of conductivity and stretchability.

Our experimental results indicate that these CuLMCs exhibit several prominent features such as high conductivity (up to 77,000 S/cm), high stretchability (up to 180%), strain-insensitivity, and cyclic stability. For flexible electronics applications, the current target performance of development is 40,000-60,000 S/cm conductivity (10% of copper) under 30% stretch. Some of our CuLMCs can achieve conductivity around 60,000 S/cm under 45-70% stretch, which are remarkable values for soft conductors. In addition, using a similar design, we also achieve strain-insensitive Joule heating behavior for strain up to 140%. In brief, CuLMCs have pushed the current limit of soft conductors in terms of conductivity and stretchability. Notably, we also discovered that adding a carbon coating on the copper network will suppress corrosion and increase the lifespan of the materials. Overall, the ultra-high and strain-insensitive conductivity, high stretchability, and cyclic stability have enabled CuLMCs promising applications in soft and flexible electronics, soft sensors, soft robotics, stretchable Joule heaters, etc. Some potential applications have been demonstrated in this work.

Future research is much needed for the manufacturing of these hybrid woven network composites with finer feature sizes to broaden their applications in stretchable electronics. In addition, it would also be very interesting to discover other microstructural designs for the woven networks towards better performance.

ASSOCIATED CONTENT

Supporting Information

The Supporting Information is available free of charge on the ACS Publications website.

Theoretical modeling of CuLMC; Data of woven mesh (Table S1); Electrical conductivity data and comparison (Tables S2, S5-S6, Figures S12); Overview of mechanism and performance (Figures S5-S6); Electromechanical behaviors of CuLMCs (Figures S7-S8, S10); Testing setup and demo (Figure S9, S11) ; Joule heating behaviors (Figures S13-S15, Table S7); SEM, EDS, and optical images (Figures S16-S18).

AUTHOR INFORMATION

Corresponding Author

Pu Zhang − *Department of Mechanical Engineering, State University of New York at Binghamton, Binghamton, NY 13902, United States;* orcid.org/0000-0001-9122-8382*;* Email: pzhang@binghamton.edu

Authors

Aminur Rahman− *Department of Mechanical Engineering, State University of New York at Binghamton, Binghamton, NY 13902, United States*

Mohammad Madadi− *Department of Mechanical Engineering, State University of New York at Binghamton, Binghamton, NY 13902, United States*

Jiexian Ma− *Department of Mechanical Engineering, State University of New York at Binghamton, Binghamton, NY 13902, United States*

Author Contributions

P.Z. supervised the project and revised the manuscript. A.R. and P.Z. introduced the concept. A.R. and J.M. designed the experimental methods. A.R. performed all experiments. M.M. performed simulations. A.R. wrote the first draft. All authors contributed to the review of the manuscript.

Notes

The authors declare no competing financial interest.

ACKNOWLEDGMENTS

This work was supported by the National Science Foundation through the award CMMI-2143297. The authors also thank the support from the Small Scale Systems Integration and Packaging (S3IP) Center of Excellence, funded by the New York Empire State Development's Division of Science, Technology, and Innovation.

REFERENCES

(1) Kaltenbrunner, M.; Sekitani, T.; Reeder, J.; Yokota, T.; Kuribara, K.; Tokuhara, T.; Drack, M.; Schwödiauer, R.; Graz, I.; Bauer-Gogonea, S.; Bauer, S.; Someya, T. An Ultra-Lightweight Design for Imperceptible Plastic Electronics. *Nature* **2013**, *499* (7459), 458–463. https://doi.org/10.1038/nature12314.

(2) Dickey, M. D. Stretchable and Soft Electronics Using Liquid Metals. *Adv. Mater.* **2017**, *29* (27), 1606425. https://doi.org/10.1002/adma.201606425.

(3) Won, D.; Bang, J.; Choi, S. H.; Pyun, K. R.; Jeong, S.; Lee, Y.; Ko, S. H. Transparent Electronics for Wearable Electronics Application. *Chem. Rev.* **2023**, *123* (16), 9982–10078. https://doi.org/10.1021/acs.chemrev.3c00139.

(4) Zhao, Z.; Xia, K.; Hou, Y.; Zhang, Q.; Ye, Z.; Lu, J. Designing Flexible, Smart and Self-Sustainable Supercapacitors for Portable/Wearable Electronics: From Conductive Polymers. *Chem. Soc. Rev.* **2021**, *50* (22), 12702–12743. https://doi.org/10.1039/D1CS00800E.

(5) Zhang, L.; Wang, Y.; Gui, J.; Wang, X.; Li, R.; Liu, W.; Sun, C.; Zhao, X.; Guo, S. Efficient Welding of Silver Nanowires Embedded in a Poly(Vinylidene Fluoride) Film for Robust Wearable Electronics. *Adv. Mater. Technol.* **2019**, *4* (2), 1800438. https://doi.org/10.1002/admt.201800438.

(6) Cheong, H.-G.; Triambulo, Ross. E.; Lee, G.-H.; Yi, I.-S.; Park, J.-W. Silver Nanowire Network Transparent Electrodes with Highly Enhanced Flexibility by Welding for Application in Flexible Organic Light-Emitting Diodes. *ACS Appl. Mater. Interfaces* **2014**, *6* (10), 7846–7855. https://doi.org/10.1021/am5011354.

(7) Celle, C.; Mayousse, C.; Moreau, E.; Basti, H.; Carella, A.; Simonato, J.-P. Highly Flexible Transparent Film Heaters Based on Random Networks of Silver Nanowires. *Nano Res.* **2012**, *5* (6), 427–433. https://doi.org/10.1007/s12274-012-0225-2.

(8) Sorel, S.; Bellet, D.; Coleman, J. N. Relationship between Material Properties and Transparent Heater Performance for Both Bulk-like and Percolative Nanostructured Networks. *ACS Nano* **2014**, *8* (5), 4805–4814. https://doi.org/10.1021/nn500692d.

(9) Ji, S.; He, W.; Wang, K.; Ran, Y.; Ye, C. Thermal Response of Transparent Silver Nanowire/PEDOT:PSS Film Heaters. *Small* **2014**, *10* (23), 4951–4960. https://doi.org/10.1002/smll.201401690.

(10) Kang, H.; Song, S.-J.; Sul, Y. E.; An, B.-S.; Yin, Z.; Choi, Y.; Pu, L.; Yang, C.-W.; Kim, Y. S.; Cho, S. M.; Kim, J.-G.; Cho, J. H. Epitaxial-Growth-Induced Junction Welding of Silver Nanowire Network Electrodes. *ACS Nano* **2018**, *12* (5), 4894–4902. https://doi.org/10.1021/acsnano.8b01900.

(11) Zhao, Y.; Kim, A.; Wan, G.; Tee, B. C. K. Design and Applications of Stretchable and Self-Healable Conductors for Soft Electronics. *Nano Converg.* **2019**, *6* (1), 25. https://doi.org/10.1186/s40580-019-0195-0.

(12) Yun, G.; Tang, S.-Y.; Lu, H.; Zhang, S.; Dickey, M. D.; Li, W. Hybrid-Filler Stretchable Conductive Composites: From Fabrication to Application. *Small Sci.* **2021**, *1* (6), 2000080. https://doi.org/10.1002/smsc.202000080.

(13) Ma, J.; Liu, Z.; Nguyen, Q.-K.; Zhang, P. Lightweight Soft Conductive Composites Embedded with Liquid Metal Fiber Networks. *Adv. Funct. Mater. n/a* (n/a), 2308128. https://doi.org/10.1002/adfm.202308128.

(14) Won, P.; Kim, K. K.; Kim, H.; Park, J. J.; Ha, I.; Shin, J.; Jung, J.; Cho, H.; Kwon, J.; Lee, H.; Ko, S. H. Transparent Soft Actuators/Sensors and Camouflage Skins for Imperceptible Soft Robotics. *Adv. Mater.* **2021**, *33* (19), 2002397. https://doi.org/10.1002/adma.202002397.
(15) Yang, Y.; Wu, Y.; Li, C.; Yang, X.; Chen, W. Flexible Actuators for Soft Robotics. *Adv. Intell. Syst.* **2020**, *2* (1), 1900077. https://doi.org/10.1002/aisy.201900077.
(16) Wang, J.; Gao, D.; Lee, P. S. Recent Progress in Artificial Muscles for Interactive Soft Robotics. *Adv. Mater.* **2021**, *33* (19), 2003088. https://doi.org/10.1002/adma.202003088.
(17) Park, M.; Park, J.; Jeong, U. Design of Conductive Composite Elastomers for Stretchable Electronics. *Nano Today* **2014**, *9* (2), 244–260. https://doi.org/10.1016/j.nantod.2014.04.009.
(18) Zhang, Y.; Zhang, Y.; Zhou, J.; Zhang, D.; Lin, H.; Chen, Y.; Li, Y.; Xiong, J. Stretchable Composite Conductive Fibers for Wearables. *Adv. Mater. Technol.* **2023**, *8* (6), 2201442. https://doi.org/10.1002/admt.202201442.
(19) Choi, S.; Han, S. I.; Kim, D.; Hyeon, T.; Kim, D.-H. High-Performance Stretchable Conductive Nanocomposites: Materials, Processes, and Device Applications. *Chem. Soc. Rev.* **2019**, *48* (6), 1566–1595. https://doi.org/10.1039/C8CS00706C.
(20) Wang, J.; Ye, T.; Jiao, Y.; Ren, W.; Li, Y.; Li, X.; Li, Y.; Li, D.; Li, F.; Wang, Y.; Song, J.; Zou, K.; Mao, W.; Wu, M.; Tan, R.; Lu, J.; He, E.; Wang, L.; Chen, H.; Li, L.; Li, Q.; Bai, C.; Gao, R.; Ren, J.; Li, W.; Cao, Y.; Zhang, Y. A Metalgel with Liquid Metal Continuum Immobilized in Polymer Network. *Adv. Mater.* **2024**, *36* (49), 2409137. https://doi.org/10.1002/adma.202409137.
(21) Zhao, Y.; Ohm, Y.; Liao, J.; Luo, Y.; Cheng, H.-Y.; Won, P.; Roberts, P.; Carneiro, M. R.; Islam, M. F.; Ahn, J. H.; Walker, L. M.; Majidi, C. A Self-Healing Electrically Conductive Organogel Composite. *Nat. Electron.* **2023**, *6* (3), 206–215. https://doi.org/10.1038/s41928-023-00932-0.
(22) Gu, W.; Guo, Q.; Zhang, Y.; Li, Y.; Zhang, Q.; Li, K.; Hou, C.; Wang, H. Activation-Independent Biphasic Liquid Metal Conductor Enables Multilayer Stretchable Electronics. *Mater. Today* **2025**. https://doi.org/10.1016/j.mattod.2025.05.020.
(23) Yu, R.; Wu, L.; Yang, Z.; Wu, J.; Chen, H.; Pan, S.; Zhu, M. Dynamic Liquid Metal–Microfiber Interlocking Enables Highly Conductive and Strain-Insensitive Metastructured Fibers for Wearable Electronics. *Adv. Mater.* **2025**, *37* (6), 2415268. https://doi.org/10.1002/adma.202415268.
(24) Choi, S.; Han, S. I.; Jung, D.; Hwang, H. J.; Lim, C.; Bae, S.; Park, O. K.; Tschabrunn, C. M.; Lee, M.; Bae, S. Y.; Yu, J. W.; Ryu, J. H.; Lee, S.-W.; Park, K.; Kang, P. M.; Lee, W. B.; Nezafat, R.; Hyeon, T.; Kim, D.-H. Highly Conductive, Stretchable and Biocompatible Ag–Au Core–Sheath Nanowire Composite for Wearable and Implantable Bioelectronics. *Nat. Nanotechnol.* **2018**, *13* (11), 1048–1056. https://doi.org/10.1038/s41565-018-0226-8.
(25) Lee, W.; Kim, H.; Kang, I.; Park, H.; Jung, J.; Lee, H.; Park, H.; Park, J. S.; Yuk, J. M.; Ryu, S.; Jeong, J.-W.; Kang, J. Universal Assembly of Liquid Metal Particles in Polymers Enables Elastic Printed Circuit Board. *Science* **2022**, *378* (6620), 637–641. https://doi.org/10.1126/science.abo6631.
(26) Parida, K.; Thangavel, G.; Cai, G.; Zhou, X.; Park, S.; Xiong, J.; Lee, P. S. Extremely Stretchable and Self-Healing Conductor Based on Thermoplastic Elastomer for All-Three-Dimensional Printed Triboelectric Nanogenerator. *Nat. Commun.* **2019**, *10* (1), 2158. https://doi.org/10.1038/s41467-019-10061-y.

(27) Xu, F.; Zhu, Y. Highly Conductive and Stretchable Silver Nanowire Conductors. *Adv. Mater.* **2012**, *24* (37), 5117–5122. https://doi.org/10.1002/adma.201201886.
(28) Miyamoto, A.; Lee, S.; Cooray, N. F.; Lee, S.; Mori, M.; Matsuhisa, N.; Jin, H.; Yoda, L.; Yokota, T.; Itoh, A.; Sekino, M.; Kawasaki, H.; Ebihara, T.; Amagai, M.; Someya, T. Inflammation-Free, Gas-Permeable, Lightweight, Stretchable on-Skin Electronics with Nanomeshes. *Nat. Nanotechnol.* **2017**, *12* (9), 907–913. https://doi.org/10.1038/nnano.2017.125.
(29) Kayaharman, M.; Argasinski, H.; Atkinson, J.; Zhang, K.; Zhou, Y. N.; Goldthorpe, I. A. Enhancing and Understanding the High Stretchability of Printable, Conductive Silver Nanowire Ink. *J. Electron. Mater.* **2023**, *52* (7), 4634–4643. https://doi.org/10.1007/s11664-023-10417-7.
(30) Zrnic, D.; Swatik, D. S. On the Resistivity and Surface Tension of the Eutectic Alloy of Gallium and Indium. *J. Common Met.* **1969**, *18* (1), 67–68. https://doi.org/10.1016/0022-5088(69)90121-0.
(31) Ma, R.; Kang, B.; Cho, S.; Choi, M.; Baik, S. Extraordinarily High Conductivity of Stretchable Fibers of Polyurethane and Silver Nanoflowers. *ACS Nano* **2015**, *9* (11), 10876–10886. https://doi.org/10.1021/acsnano.5b03864.
(32) Cao, C.; Huang, X.; Lv, D.; Ai, L.; Chen, W.; Hou, C.; Yi, B.; Luo, J.; Yao, X. Ultrastretchable Conductive Liquid Metal Composites Enabled by Adaptive Interfacial Polarization. *Mater. Horiz.* **2021**, *8* (12), 3399–3408. https://doi.org/10.1039/D1MH00924A.
(33) Park, S.; Thangavel, G.; Parida, K.; Li, S.; Lee, P. S. A Stretchable and Self-Healing Energy Storage Device Based on Mechanically and Electrically Restorative Liquid-Metal Particles and Carboxylated Polyurethane Composites. *Adv. Mater.* **2019**, *31* (1), 1805536. https://doi.org/10.1002/adma.201805536.
(34) Chen, G.; Wang, H.; Guo, R.; Duan, M.; Zhang, Y.; Liu, J. Superelastic EGaIn Composite Fibers Sustaining 500% Tensile Strain with Superior Electrical Conductivity for Wearable Electronics. *ACS Appl. Mater. Interfaces* **2020**, *12* (5), 6112–6118. https://doi.org/10.1021/acsami.9b23083.
(35) Dong, S.; Zhu, X.; Guo, Y.; Zhang, P.; Ma, G.; Li, W.; Zhang, S. A Stretch-Insensitive Pressure Sensor Based on Liquid Metal Composite with a Hierarchical Conductive Network. *ACS Appl. Mater. Interfaces* **2025**, *17* (27), 39480–39489. https://doi.org/10.1021/acsami.5c03997.
(36) Wang, Q.; Sun, Y.; Qin, C.; Lin, Y.; Fang, T.; Yang, C.; Zhang, J.; Lu, Y.; Kong, D. Stretchable and Permeable Liquid Metal Micromeshes Featuring Strain-Insensitive Resistance Through In Situ Structural Transformations. *Adv. Mater.* **2025**, *37* (11), 2417799. https://doi.org/10.1002/adma.202417799.
(37) Lee, D. H.; Lim, T.; Pyeon, J.; Park, H.; Lee, S.-W.; Lee, S.; Kim, W.; Kim, M.; Lee, J.-C.; Kim, D.-W.; Han, S.; Kim, H.; Park, S.; Choi, Y.-K. Self-Mixed Biphasic Liquid Metal Composite with Ultra-High Stretchability and Strain-Insensitivity for Neuromorphic Circuits. *Adv. Mater.* **2024**, *36* (16), 2310956. https://doi.org/10.1002/adma.202310956.
(38) Yao, B.; Hong, W.; Chen, T.; Han, Z.; Xu, X.; Hu, R.; Hao, J.; Li, C.; Li, H.; Perini, S. E.; Lanagan, M. T.; Zhang, S.; Wang, Q.; Wang, H. Highly Stretchable Polymer Composite with Strain-Enhanced Electromagnetic Interference Shielding Effectiveness. *Adv. Mater.* **2020**, *32* (14), 1907499. https://doi.org/10.1002/adma.201907499.

(39) Fang, R.; Yao, B.; Chen, T.; Xu, X.; Xue, D.; Hong, W.; Wang, H.; Wang, Q.; Zhang, S. 3D Highly Stretchable Liquid Metal/Elastomer Composites with Strain-Enhanced Conductivity. *Adv. Funct. Mater.* **2024**, *34* (31), 2310225. https://doi.org/10.1002/adfm.202310225.
(40) Zhu, S.; So, J.-H.; Mays, R.; Desai, S.; Barnes, W. R.; Pourdeyhimi, B.; Dickey, M. D. Ultrastretchable Fibers with Metallic Conductivity Using a Liquid Metal Alloy Core. *Adv. Funct. Mater.* **2013**, *23* (18), 2308–2314. https://doi.org/10.1002/adfm.201202405.
(41) Chen, J.; Chen, X.; Su, Y.; Shen, B.; Zheng, W. Multifunctional Strain-Activated Liquid–Metal Composite Films with Electromechanical Decoupling for Stretchable Electromagnetic Shielding. *Mater. Horiz.* **2024**, *11* (24), 6381–6390. https://doi.org/10.1039/D4MH00774C.
(42) Rogers, J. A.; Someya, T.; Huang, Y. Materials and Mechanics for Stretchable Electronics. *Science* **2010**, *327* (5973), 1603–1607. https://doi.org/10.1126/science.1182383.
(43) Wang, J.; Cai, G.; Li, S.; Gao, D.; Xiong, J.; Lee, P. S. Printable Superelastic Conductors with Extreme Stretchability and Robust Cycling Endurance Enabled by Liquid-Metal Particles. *Adv. Mater.* **2018**, *30* (16), 1706157. https://doi.org/10.1002/adma.201706157.
(44) Suh, Y. D.; Jung, J.; Lee, H.; Yeo, J.; Hong, S.; Lee, P.; Lee, D.; Ko, S. H. Nanowire Reinforced Nanoparticle Nanocomposite for Highly Flexible Transparent Electrodes: Borrowing Ideas from Macrocomposites in Steel-Wire Reinforced Concrete. *J. Mater. Chem. C* **2017**, *5* (4), 791–798. https://doi.org/10.1039/C6TC04529D.
(45) Yao, S.; Zhu, Y. Nanomaterial-Enabled Stretchable Conductors: Strategies, Materials and Devices. *Adv. Mater.* **2015**, *27* (9), 1480–1511. https://doi.org/10.1002/adma.201404446.
(46) Joo, H.; Jung, D.; Sunwoo, S.-H.; Koo, J. H.; Kim, D.-H. Material Design and Fabrication Strategies for Stretchable Metallic Nanocomposites. *Small* **2020**, *16* (11), 1906270. https://doi.org/10.1002/smll.201906270.
(47) Hajalilou, A.; Silva, A. F.; Lopes, P. A.; Parvini, E.; Majidi, C.; Tavakoli, M. Biphasic Liquid Metal Composites for Sinter-Free Printed Stretchable Electronics. *Adv. Mater. Interfaces* **2022**, *9* (5), 2101913. https://doi.org/10.1002/admi.202101913.
(48) Madadi, M.; Zhang, P. Finite-Size Effect on the Percolation and Electromechanical Behaviors of Liquid Metal Particulate Composites. *Soft Matter* **2024**, *20* (5), 1061–1069. https://doi.org/10.1039/D3SM01469J.
(49) Lim, J.-E.; Lee, S.-M.; Kim, S.-S.; Kim, T.-W.; Koo, H.-W.; Kim, H.-K. Brush-Paintable and Highly Stretchable Ag Nanowire and PEDOT:PSS Hybrid Electrodes. *Sci. Rep.* **2017**, *7* (1), 14685. https://doi.org/10.1038/s41598-017-14951-3.
(50) Feng, P.; Ye, Z.; Wang, Q.; Chen, Z.; Wang, G.; Liu, X.; Li, K.; Zhao, W. Stretchable and Conductive Composites Film with Efficient Electromagnetic Interference Shielding and Absorptivity. *J. Mater. Sci.* **2020**, *55* (20), 8576–8590. https://doi.org/10.1007/s10853-019-04172-6.
(51) Kang, H.; Yi, G.-R.; Kim, Y. J.; Cho, J. H. Junction Welding Techniques for Metal Nanowire Network Electrodes. *Macromol. Res.* **2018**, *26* (12), 1066–1073. https://doi.org/10.1007/s13233-018-6150-9.
(52) Wang, Y.; Zhang, L.; Wang, D. Ultrastretchable Hybrid Electrodes of Silver Nanowires and Multiwalled Carbon Nanotubes Realized by Capillary-Force-Induced Welding. *Adv. Mater. Technol.* **2019**, *4* (11), 1900721. https://doi.org/10.1002/admt.201900721.
(53) Woo, J. Y.; Kim, K. K.; Lee, J.; Kim, J. T.; Han, C.-S. Highly Conductive and Stretchable Ag Nanowire/Carbon Nanotube Hybrid Conductors. *Nanotechnology* **2014**, *25* (28), 285203. https://doi.org/10.1088/0957-4484/25/28/285203.

(54) Hauger, T. C.; Al-Rafia, S. M. I.; Buriak, J. M. Rolling Silver Nanowire Electrodes: Simultaneously Addressing Adhesion, Roughness, and Conductivity. *ACS Appl. Mater. Interfaces* **2013**, *5* (23), 12663–12671. https://doi.org/10.1021/am403986f.
(55) Park, J. H.; Hwang, G.-T.; Kim, S.; Seo, J.; Park, H.-J.; Yu, K.; Kim, T.-S.; Lee, K. J. Flash-Induced Self-Limited Plasmonic Welding of Silver Nanowire Network for Transparent Flexible Energy Harvester. *Adv. Mater.* **2017**, *29* (5), 1603473. https://doi.org/10.1002/adma.201603473.
(56) Yoon, S.-S.; Khang, D.-Y. Room-Temperature Chemical Welding and Sintering of Metallic Nanostructures by Capillary Condensation. *Nano Lett.* **2016**, *16* (6), 3550–3556. https://doi.org/10.1021/acs.nanolett.6b00621.
(57) Guo, R.; Wang, H.; Chen, G.; Yuan, B.; Zhang, Y.; Liu, J. Smart Semiliquid Metal Fibers with Designed Mechanical Properties for Room Temperature Stimulus Response and Liquid Welding. *Appl. Mater. Today* **2020**, *20*, 100738. https://doi.org/10.1016/j.apmt.2020.100738.
(58) Wang, S.; Liu, H.; Pan, Y.; Xie, F.; Zhang, Y.; Zhao, J.; Wen, S.; Gao, F. Performance Enhancement of Silver Nanowire-Based Transparent Electrodes by Ultraviolet Irradiation. *Nanomaterials* **2022**, *12* (17), 2956. https://doi.org/10.3390/nano12172956.
(59) Wang, S.; Tian, H.; Wang, Y.; Zuo, H.; Tao, C.; Liu, J.; Li, P.; Yang, Y.; Kou, X.; Wang, J.; Kang, W. Ruptured Liquid Metal Microcapsules Enabling Hybridized Silver Nanowire Networks towards High-Performance Deformable Transparent Conductors. *Nanoscale* **2024**, *16* (13), 6522–6530. https://doi.org/10.1039/D3NR06508A.
(60) Lide, D. R. *CRC Handbook of Chemistry and Physics, 85th Edition*; CRC Press, 2004.
(61) Kim, T.-W.; Lee, J.-S.; Kim, Y.-C.; Joo, Y.-C.; Kim, B.-J. Bending Strain and Bending Fatigue Lifetime of Flexible Metal Electrodes on Polymer Substrates. *Materials* **2019**, *12* (15), 2490. https://doi.org/10.3390/ma12152490.
(62) Kim, D.-H.; Lu, N.; Ma, R.; Kim, Y.-S.; Kim, R.-H.; Wang, S.; Wu, J.; Won, S. M.; Tao, H.; Islam, A.; Yu, K. J.; Kim, T.; Chowdhury, R.; Ying, M.; Xu, L.; Li, M.; Chung, H.-J.; Keum, H.; McCormick, M.; Liu, P.; Zhang, Y.-W.; Omenetto, F. G.; Huang, Y.; Coleman, T.; Rogers, J. A. Epidermal Electronics. *Science* **2011**, *333* (6044), 838–843. https://doi.org/10.1126/science.1206157.
(63) Lee, J.; Wu, J.; Ryu, J. H.; Liu, Z.; Meitl, M.; Zhang, Y.-W.; Huang, Y.; Rogers, J. A. Stretchable Semiconductor Technologies with High Areal Coverages and Strain-Limiting Behavior: Demonstration in High-Efficiency Dual-Junction GaInP/GaAs Photovoltaics. *Small* **2012**, *8* (12), 1851–1856. https://doi.org/10.1002/smll.201102437.
(64) Cui, Y.; Ding, Y.; Xu, S.; Yang, Z.; Zhang, P.; Rao, W.; Liu, J. Liquid Metal Corrosion Effects on Conventional Metallic Alloys Exposed to Eutectic Gallium–Indium Alloy Under Various Temperature States. *Int. J. Thermophys.* **2018**, *39* (10), 113. https://doi.org/10.1007/s10765-018-2440-x.
(65) Mu, G.; Qu, W.; Zhu, H.; Zhuang, H.; Zhang, Y. Low Temperature Cu/Ga Solid–Liquid Inter-Diffusion Bonding Used for Interfacial Heat Transfer in High-Power Devices. *Metals* **2020**, *10* (9), 1223. https://doi.org/10.3390/met10091223.
(66) Liu, G.; He, D.; Liu, J.; Xie, H.; Chen, Z.; Wei, C.; Xu, X.; Wang, P. Influencing Factors for Resistance Performance of Cu/C Composites to Liquid Ga Corrosion. *Mater. Today Commun.* **2023**, *35*, 105999. https://doi.org/10.1016/j.mtcomm.2023.105999.
(67) Liao, Z.; Hossain, M.; Yao, X.; Navaratne, R.; Chagnon, G. A Comprehensive Thermo-Viscoelastic Experimental Investigation of Ecoflex Polymer. *Polym. Test.* **2020**, *86*, 106478. https://doi.org/10.1016/j.polymertesting.2020.106478.

For Table of Contents Only

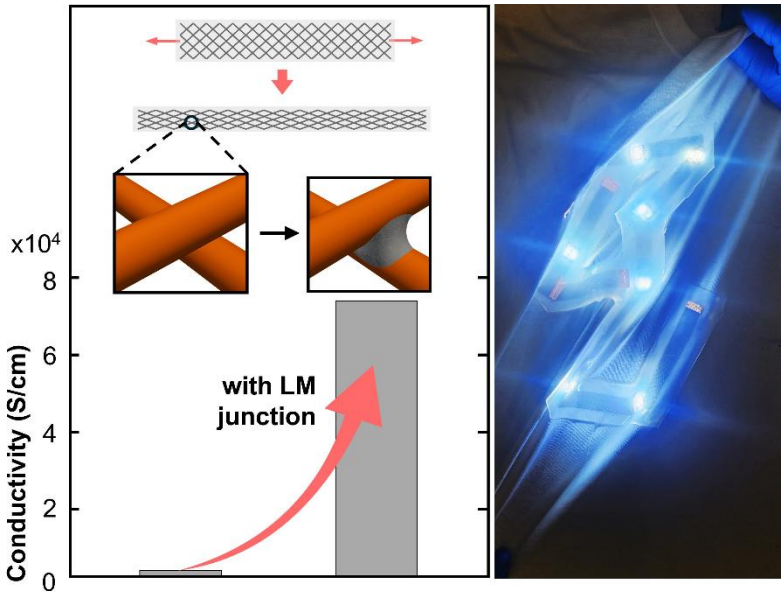

Supporting Information

Overcoming Conductivity-Stretchability Tradeoff in Soft Conductive Composites Through Liquid Metal Junctions

Aminur Rahman[a], Mohammad Madadi[a], Jiexian Ma[a], Pu Zhang[a]*

[a] *Department of Mechanical Engineering, State University of New York at Binghamton, Binghamton, NY 13902, United States*

* Email: pzhang@binghamton.edu

Table of Contents

- **Table S1.** Specifics of the woven copper mesh used in this work ……. 4
- **Table S2.** Survey of electrical conductivity of soft/stretchable conductive composites……. 5
- **Stretchability enhancement of CuLMCs by prestrain** ……...….. 7
- **Figure S1.** Stretchability enhancement by tuning the angle of the mesh through prestrain..…..7
- **Stretchability-conductivity relation of angled CuLMCs**…… 8
- **Table S3.** Sheet resistance and thickness of the CuLMCs ……. 9
- **Figure S2**. Schematic of mesh geometry and unit cell before and after applying prestrain ε to change the intersectional angle…… 10
- **Figure S3.** Schematic of crossed and angled mesh microstructures and unit cell under various deformation states…… 10
- **Table S4.** Maximum compression & maximum tension of the copper meshes by changing intersection angle……. 11
- **Figure S4.** Theoretical prediction of electrical conductivity and stretchability of prestrained CuLMCs…….. 11
- **Figure S5.** The electrical conductivity of copper mesh composites (CuCs), LM-coated composites (CuLMCs), and prestrained CuLMCs (angled mesh) ……. 12
- **Figure S6.** Working mechanism and performance of the strain-insensitive conductivity behavior of mesh 40 CuLMCs ……...……13
- **Figure S7.** Additional electromechanical behavior of mesh 40 CuLMC composites before and after LM coating ……14
- **Figure S8.** Electrical conductivity of prestrained CuLMCs under stretch ……15
- **Figure S9.** Electromechanical testing setup for tension and bending test ……. 16
- **Figure S10.** Additional electromechanical behavior of mesh 40 CuLMCs during cyclic loading-unloading test …… 17
- **Figure S11.** Application of CuLMCs as stretchable and wearable interconnects mounted on textiles under extreme conditions …… 18

- **Figure S12.** Comparison of the electrical conductivity-strain relations of CuLMCs with random percolation, structure (Kirigami) and geometry-based (wrinkle/folded) composites …… 19
- **Table S5.** Electrical resistance of CuCs and CuLMCs fabricated from different mesh sizes …20
- **Table S6.** Survey of electrical conductivity of random percolation, structure, and geometry-based stretchable conductive composites ……21
- **Figure S13.** Joule heating behavior of angled mesh brass-LM composite under mechanical stretching …… 22
- **Figure S14.** Joule heating stability analysis of brass-LM composites on day 1 & day 20 …… 23
- **Figure S15.** Joule heating performance of the original (crossed mesh) and pre-compressed (angled mesh) brass-LM composite heaters ……24
- **Figure S16.** SEM images of conductive LM junction ……25
- **Figure S17.** EDS analysis of carbon coated copper mesh ……..26
- **Figure S18.** Additional optical images of 0%, -10%, -20%, and -33 prestrained mesh 40 CuLMCs ……..27
- **Table S7.** Survey of soft and stretchable composites for Joule heating applications ……28
- **References** ……..29

Table S1. Specifics of the woven copper mesh used in this work.

Mesh Size	Fiber Diameter [mm]	Mesh Thickness [mm]	Opening Rate [%]
20	0.15	0.30	77.77
30	0.11	0.22	75.70
40	0.10	0.20	70.98
60	0.075	0.15	67.71

The mesh opening rate r_A can be calculated by using the following equations.

$$r_{\mathrm{A}} = \left(\frac{a}{a+d}\right)^2 \tag{S1}$$

$$\frac{25.4\ mm}{Mesh\ size} = pitch = a + d \tag{S2}$$

where a is the mesh opening and d is the fiber diameter (both in mm).

Table S2. Survey of electrical conductivity of soft/stretchable conductive composites[†].

Material	Fabrication Method	Initial Electrical Conductivity [S/cm]	Maximum Insensitive Strain [%]	Electrical Conductivity at Maximum Insensitive Strain [S/cm]	Ref.
CuLMC Composites:					
Mesh 20 CuLMC (no prestrain)	PVD, coating	48000	40	48000	
Mesh 30 CuLMC (no prestrain)	PVD, coating	67000	30	66000	
Mesh 40 CuLMC (no prestrain)	PVD, coating	75000	25	73500	
Mesh 60 CuLMC (no prestrain)	PVD, coating	77000	22	76500	
Mesh 20 CuLMC (-50% prestrain)	PVD, coating	27000	180	27000	This work
Mesh 30 CuLMC (-35% prestrain)	PVD, coating	40000	120	40000	
Mesh 40 CuLMC (-10% prestrain)	PVD, coating	65000	45	64000	
Mesh 40 CuLMC (-20% prestrain)	PVD, coating	58000	55	57000	
Mesh 40 CuLMC (-33% prestrain)	PVD, coating	45000	100	44000	
Mesh 60 CuLMC (-26% prestrain)	PVD, coating	58000	70	58000	

[†] Three criteria were used to screen data from the literature: (1) Conductivity is higher than 1000 S/cm. (2) Conductivity is considered as strain-insensitive if it is within 10% change compared to initial conductivity. (3) Skeptical data that are physically impossible were removed.

Table S2. (continued)

Material	Fabrication Method	Initial Electrical Conductivity [S/cm]	Maximum Insensitive Strain [%]	Electrical Conductivity at Maximum Insensitive Strain [S/cm]	Ref.
LM Filler Composites:					
GaInSn PDMS	mixing, casting	16200	40	14500	[1]
EGaIn PDMS	mixing, casting	1370	50	1300	[2]
LMP PU	mixing, printing	21000	100	20000	[3]
Hard Filler Composites:					
AgNP PVDF	mixing, hot rolling	3228	5	2500	[4]
AgNW SBS	direct printing	5500	20	5200	[5]
AgNW PDMS	solution casting	5285	45	4700	[6]
Au PVP	electrospinning & vacuum deposition	5800 [a)]	10	5500	[7]
Ag-AuNW SBS	mixing, casting	41850 [b)]	0	-	[8]
Hybrid Filler Composites (i.e., solid-liquid filler):					
Ag flakes EGaIn PUA	direct printing	6250	600	5700	[9]
Ag flakes EGaInPs	direct printing	8331	100	7500	[10]
Ni-EGaIn PDMS	stencil printing	8000 [c)]	25	7000	[11]
EGaIn-Ag-SIS	direct writing	2500	400	2250	[12]
AgNW-EGaIn-PDMS	drop casting	9000	25	8000	[13]
EGaIn-Ni CPU	solution mixing	2479	100	2400	[14]

[a)]calculated from the given parameters; [b)]taken from their Ashby chart; [c)]this composite is for comparison only.

Stretchability enhancement of CuLMCs by prestrain

The interwoven copper mesh exhibits a unique microstructural geometry that can be reconfigured by adjusting the intersection angles through compression or tension. The fibers within the mesh are capable of moving freely up to a specific threshold for each geometric configuration. As depicted in **Figure S1** (a), when tension is applied to a crossed mesh with a 90^0 intersection angle, the fibers undergo a certain degree of rotation before fiber pullout occurs. For an angled mesh (pre-compression), this geometric adjustment enables the mesh to achieve a higher degree of stretchability when subjected to tension, owing to the increased freedom of rotation at the intersection angles. Therefore, CuLMCs made of angled copper mesh have improved stretchability, although some conductivity will be sacrificed.

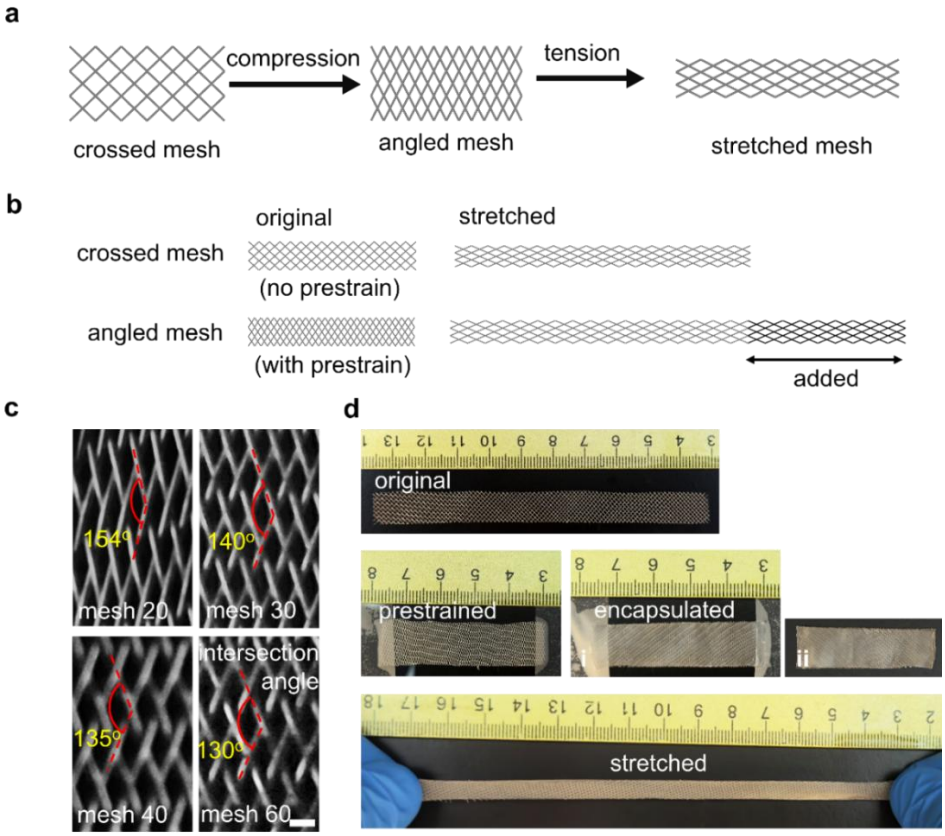

Figure S1. Stretchability enhancement by tuning the angle of the mesh through prestrain. (a) Schematic of crossed mesh and angled mesh geometry. The intersectional angle in the crossed mesh is 90^0 and increases with compression (folding) and reduces with tension (unfolding). (b) Schematic of stretchability enhancement by tuning the intersectional angle in the mesh. Angled mesh is able to provide extended stretchability by applying prestrain. (c) Optical images of different angled mesh geometry under maximum compression (prestrain). The intersection angle for mesh 20, 30, 40, and 60 are respectively 154^0, 140^0, 135^0, and 130^0. Scale bar 1mm. (d) Optical images of mesh 20 CuLMC in different states. The original mesh is pre-compressed with -50% strain (prestrain) before encapsulation in PDMS. No folds/wrinkles are present in the microstructure before and after embedding.

Stretchability-Conductivity Relation of Angled CuLMCs

The relationship of prestrain applied by rotation angle, conductivity, and stretchability can be established from the following theoretical analysis.

Conductivity-Prestrain Relation

In crossed mesh geometry, the material conductivity can be expressed as Equation (S3) below,

$$\sigma^E = \frac{1}{R}\frac{L}{Wt} \qquad \text{(crossed mesh)} \tag{S3}$$

where t is the sample thickness, R is resistance, L is the length, and W is the width. To simplify the calculation, a unit cell is considered from the composite sample. Normally under prestrain ε, the unit cell will deform but the fiber length is constant, as illustrated in **Figure S2**.

As shown in Figure S2, after applying prestrain (pre-compression), the total length and width of the sample change to $L\ (1+\varepsilon\ )$ and $W\sqrt{1-\varepsilon^2-2\varepsilon}$, while the thickness *t* and resistance *R* are almost constant. Then following Equation (S3), the material conductivity of a prestrained mesh is

$$\sigma^E = \frac{1}{R}\frac{L}{Wt}\frac{1+\varepsilon}{\sqrt{1-\varepsilon^2-2\varepsilon}} \tag{S4}$$

In case with no prestrain ($\varepsilon = 0$), Equation (S4) degenerates to Equation (S3). Here, $\frac{R}{L/W} = R_s$ is known as the sheet resistance (Ω/sq). The sheet resistance and thickness of the copper meshes are measured and outlined in **Table S3**.

According to **Equation (S4)**, the electrical conductivity generally decreases with the increase of prestrain under compression. The mesh 60 CuLMC exhibits the highest electrical conductivity, and the mesh 20 CuLMC shows the lowest. The trends are presented in **Figure S4 (a)**, **Figure S5 (b)**, and **Figure S8**.

Stretchability-Prestrain Relation

The stretchability of a square mesh can be enhanced by applying prestrain (pre-compression) by altering the angle. The mechanism is illustrated in **Figure S3** and explained below. As illustrated in **Figure S3**, a mesh unit cell has three deformation states: maximum compression, maximum tension, and prestrain. The maximum compression state and maximum tension state are two extreme scenarios when fiber locking occurs and no further deformation is feasible. These two states are actually identical after 90° rotation. Under prestrain ε, the length of a unit cell changes to l_3. The stretchability of a prestrained mesh is measured from the prestrain state to the maximum tension state, as $\varepsilon_{max} = \frac{l_2 - l_3}{l_3}$. Under pre-compression, l_3 decreases so that ε_{max} can be increased.

The stretchability-prestrain relation can be derived theoretically below. Designating $\bar{\varepsilon}_C$ the maximum compression strain and $\bar{\varepsilon}_T$ the maximum tension strain, the length of the deformed unit cell can be obtained as shown in **Figure S3**. Considering that the fiber length is constant, $\bar{\varepsilon}_C$ and $\bar{\varepsilon}_T$ follow a simple relation as

$$\bar{\varepsilon}_T = \sqrt{1-\bar{\varepsilon}_C{}^2-2\bar{\varepsilon}_C} - 1 \tag{S5}$$

where the maximum compression strain $\bar{\varepsilon}_C$ needs to be calibrated from experiment. Table S4 presents the measured $\bar{\varepsilon}_C$ values for different meshes and the predicted $\bar{\varepsilon}_T$ using **Equation (S5)**. Finally, the stretchability of a prestrained mesh is given by

$$\varepsilon_{max} = \frac{l_2 - l_3}{l_3} = \frac{\bar{\varepsilon}_T - \varepsilon}{1 + \varepsilon} \tag{S6}$$

The stretchability-prestrain relation in **Equation (S6)** is illustrated in **Figure S4**. The results show that applying prestrain can increase the stretchability dramatically. **Figure S4**, together with **Equation (S4)** and **(S6)**, can be used to design the conductivity and stretchability of CuLMCs using prestrain engineering.

Table S3. Sheet resistance and thickness of the CuLMCs.

Composite	Parameters	Experimental Value
Mesh 20	Sheet Resistance, R_s	0.000657 Ω/sq
	Thickness, t	300 μm
Mesh 30	Sheet Resistance, R_s	0.000667 Ω/sq
	Thickness, t	220 μm
Mesh 40	Sheet Resistance, R_s	0.000685 Ω/sq
	Thickness, t	200 μm
Mesh 60	Sheet Resistance, R_s	0.000806 Ω/sq
	Thickness, t	160 μm

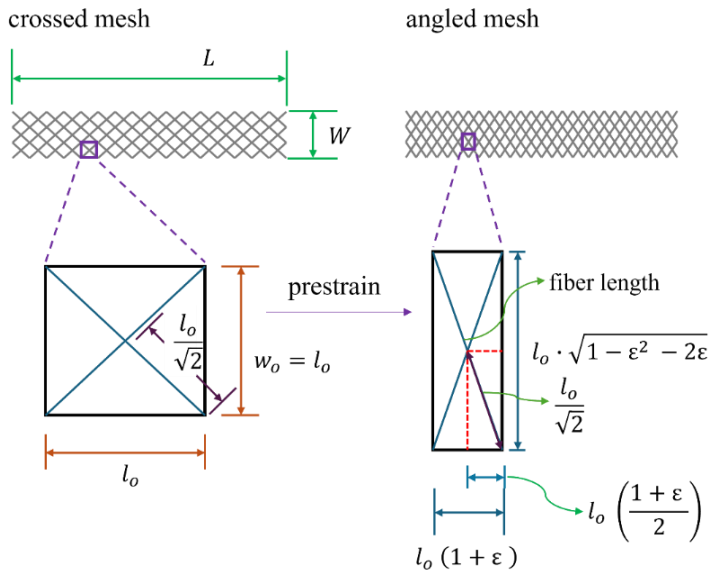

Figure S2. Schematic of mesh geometry and unit cell before and after applying prestrain ε to change the intersectional angle.

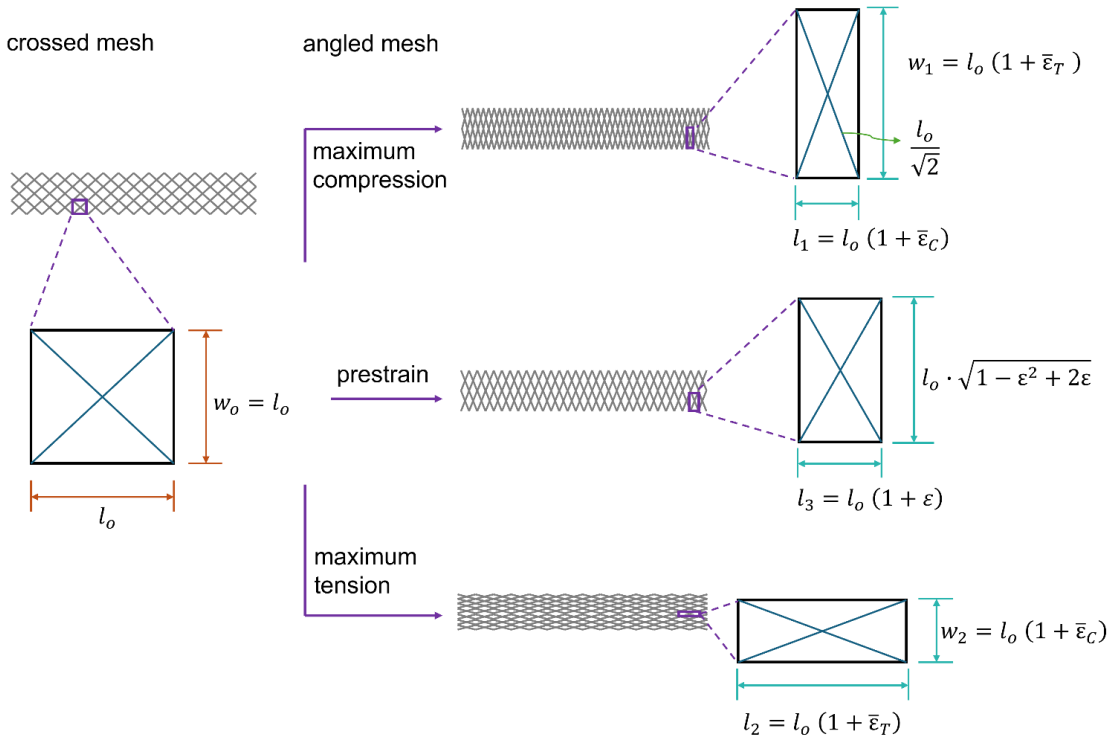

Figure S3. Schematic of crossed and angled mesh microstructures and unit cell under various deformation states. The stretchability ε_{max} is measured from the prestrain state to the maximum tension state, defined as $\varepsilon_{max} = \frac{l_2 - l_3}{l_3}$.

Table S4. Maximum compression & maximum tension of the copper meshes by changing intersection angle.

Composite	Maximum compression ($\bar{\varepsilon}_C$)	Maximum tension ($\bar{\varepsilon}_T$)
Mesh 20	-0.50	0.32
Mesh 30	-0.35	0.26
Mesh 40	-0.33	0.25
Mesh 60	-0.26	0.21

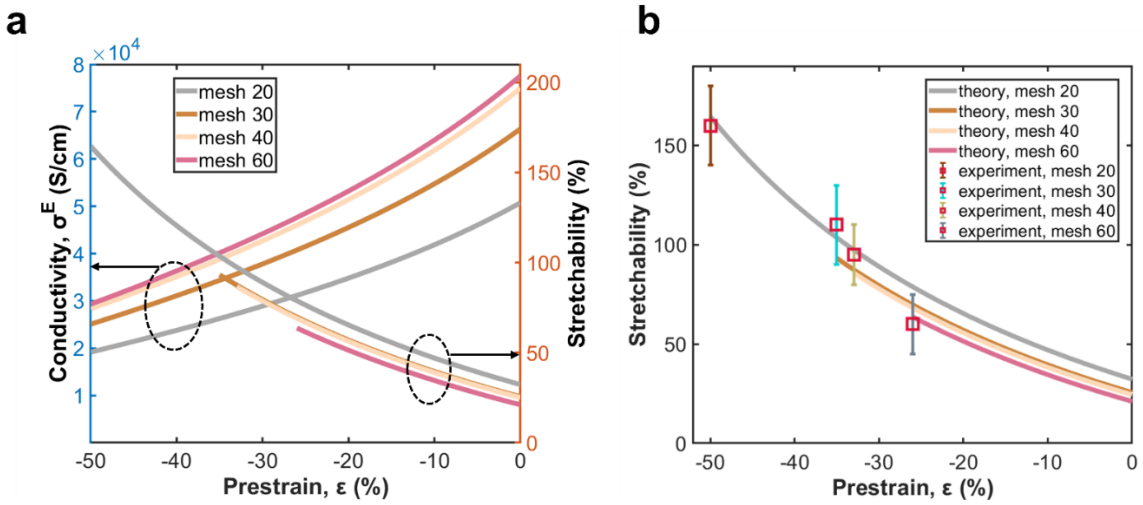

Figure S4. Theoretical prediction of electrical conductivity and stretchability of prestrained CuLMCs. (a) Theoretical prediction of the conductivity-prestrain and stretchability-prestrain relations of composites with different mesh sizes. (b) Comparison of theoretical prediction and experimental measurement of the stretchability-prestrain relation. The stretchability is considered up to the fiber rotation stage.

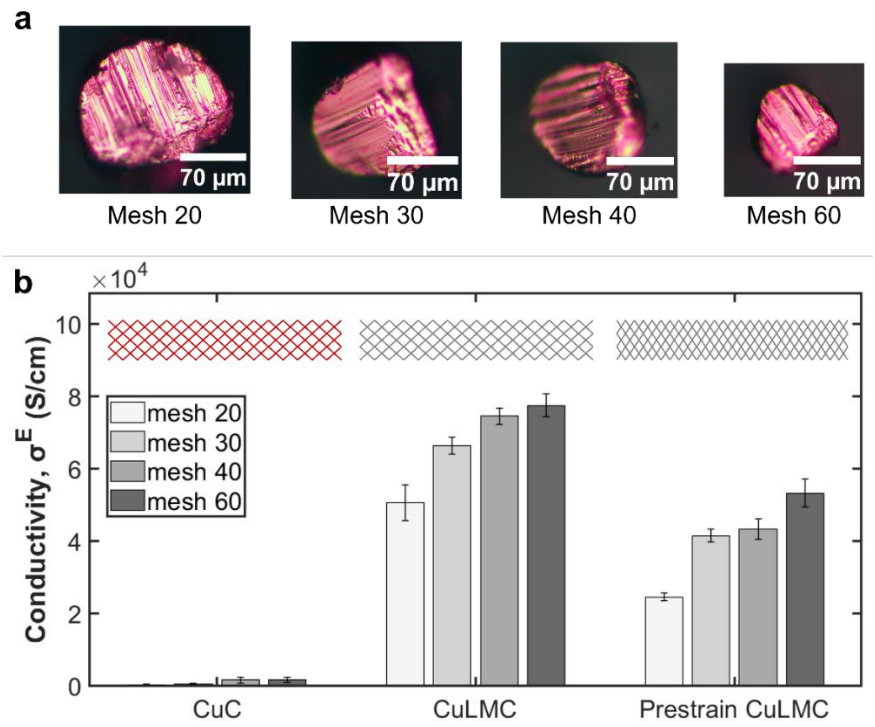

Figure S5. The electrical conductivity of copper mesh composites (CuCs), LM-coated composites (CuLMCs), and prestrained (angled mesh) CuLMCs. (a) Optical microscopy images of fiber cross-sections for different mesh sizes. The diameter of mesh 20, 30, 40, and 60 is 150µm, 110µm, 100µm, and 75µm, respectively. (b) The electrical conductivity of CuCs, CuLMCs, and prestrained CuLMCs. Due to high junction resistance, the CuCs exhibit poor electrical conductivity. The LM junction reduced the contact resistance significantly and achieved 20- to 60-fold improvement in conductivity. The prestrained composites also show remarkable improvement in electrical conductivity, although the conductivity is slightly lower as tradeoff of better stretchability.

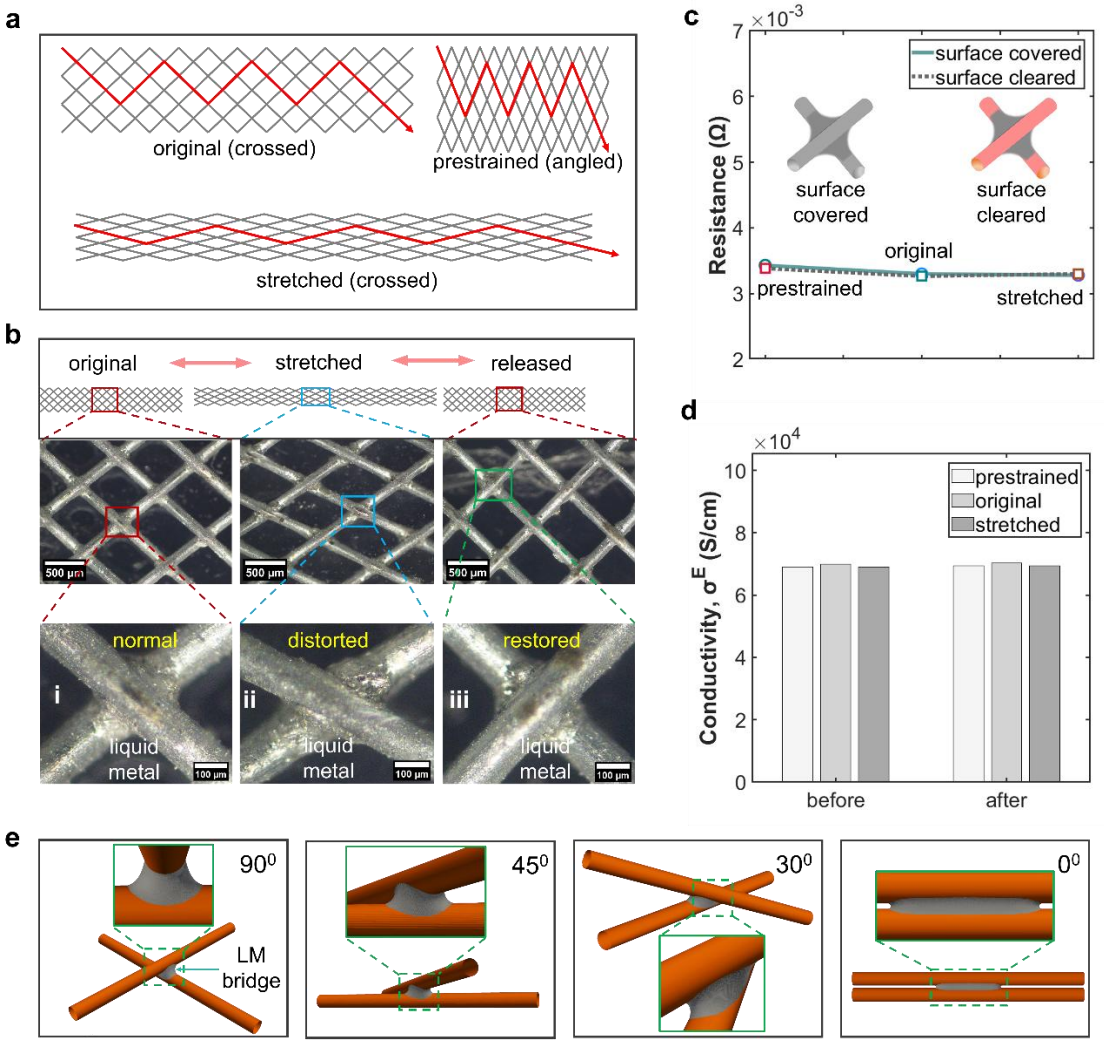

Figure S6. The working mechanism and performance of the strain-insensitive conductivity behavior of mesh 40 CuLMCs. (a) Illustration of a hypothetical conductive pathway (red arrow) in the composite in the original, prestrained, and stretched states. The total length of the conductive pathway remains equal in every state, giving rise to the strain-insensitive conductivity behavior. (b) Schematic and optical images of the microstructure evolution at the original, stretched, and released states. The geometry expands under tensile strain (stretched up to 25% strain) and reverts to its original configuration upon release. The LM bridge (bottom row) in the junction area typically distorts under stretching and recovers upon release of the stretching. (c) The resistance trend of mesh 40 CuLMC in all three states. The overall resistance remains steady and does not fluctuate as long as the length of the conductive is maintained constant. Two different types of samples were analyzed: surface covered (coated with LM), and surface cleared (coated with LM and then polished & wiped with the isopropyl alcohol to remove LM from the surface area). The removal of LM from the surface has very marginal impact on the electrical properties. (d) The electrical conductivity of mesh 40 before and after encapsulation in PDMS. (e) LM bridge morphologies obtained from Surface Evolver simulations for a LM droplet with a volume of 0.3 micro liter between two fibers with 90^0, 45^0, 30^0, and 0^0 rotation; radius of fibers is 0.3µm and height is 10µm; contact angle is considered 10^0.

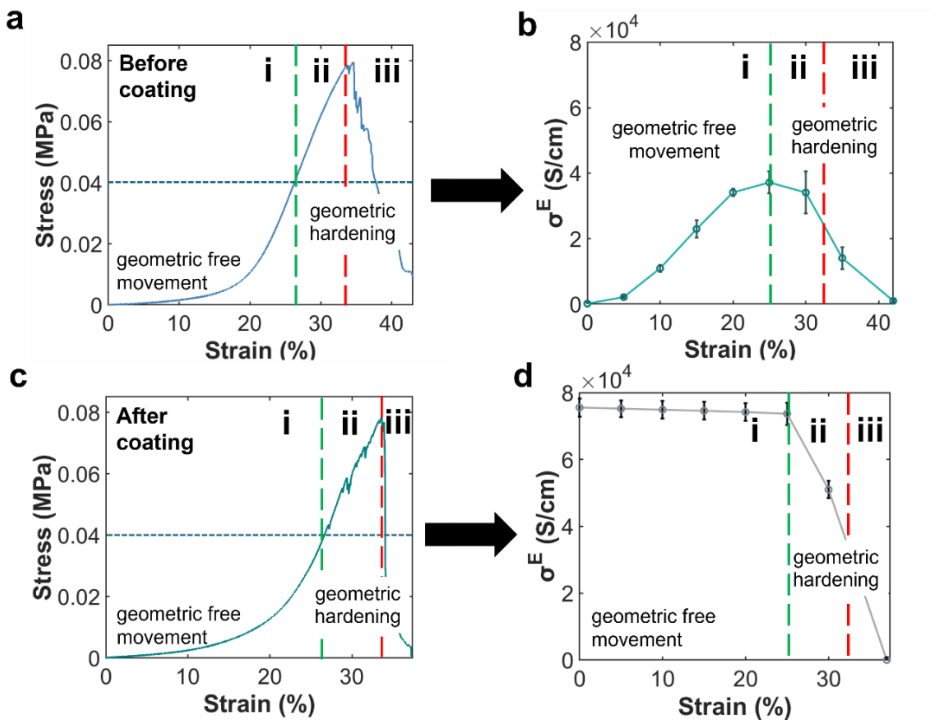

Figure S7. Additional electromechanical behavior of mesh 40 CuLMC composites before and after LM coating. The conductivity behavior is different before and after LM coating. (a) Stress-strain curve before coating. (b) Conductivity-strain curve before coating. (c) Stress-strain curve after coating. (d) Conductivity-strain curve after coating. Before coating, it lacks junction connectivity so the contact resistance is high; therefore, conductivity is poor and strain-sensitive. The LM coating improved the conductivity and strain insensitivity. From the microstructure perspective, composites are stretchable to a certain limit until geometric hardening and fiber interlocking start. There are three different stages during mechanical stretch: i) fiber rotation, ii) fiber interlocking, and iii) fiber pullout failure. The electrical conductivity in the geometric free movement region is stable for coated composites and gradually increases to the peak for uncoated composites. Beyond that, conductivity starts to reduce for both cases, evidencing accumulating damage in the composites.

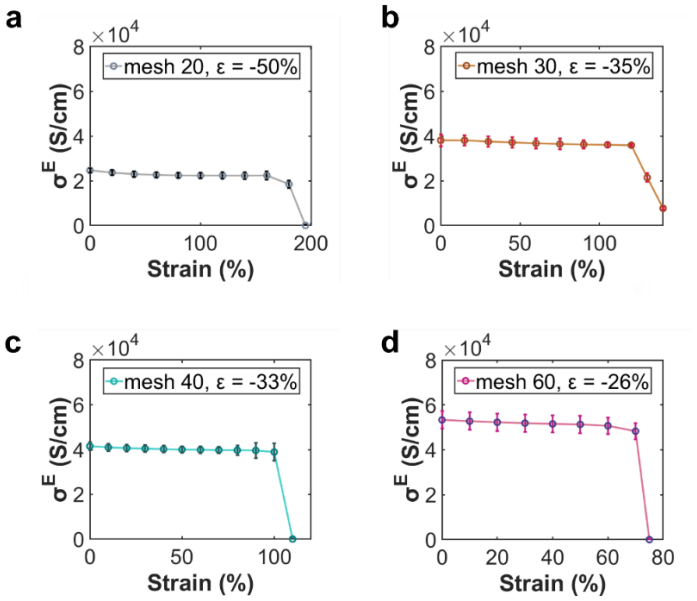

Figure S8. Electrical conductivity of prestrained CuLMCs under stretch: (a) Mesh 20; (b) Mesh 30; (c) Mesh 40; (d) Mesh 60. Among these samples, mesh 20 CuLMC has the lowest electrical conductivity and mesh 60 CuLMC has the highest. The prestrain strategy also improved the stretchability and it is respectively 180% for mesh 20, 110% for mesh 30, 90% for mesh 40, and 60% for mesh 60 CuLMC.

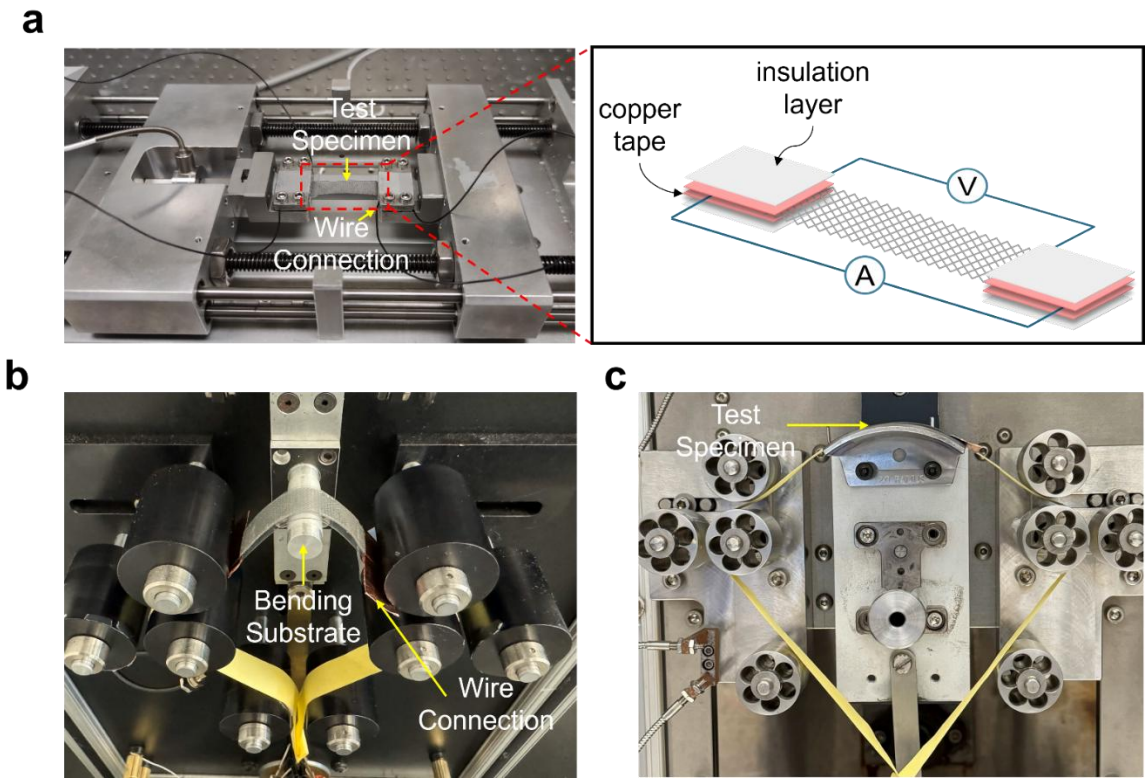

Figure S9. Electromechanical testing setup for tension and bending test. (a) Four wire resistance measurement during tensile testing. (b) Bending test setup (smaller substrate radius, bending strain 2.5 to 4%, the device is assembled by Veeder-root) coupled with electrical measurement. (c) Bending test setup (larger substrate radius, bending strain 0.5 to 2%, assembled by associated environmental systems BHK4108) coupled with electrical measurement. Tensile bending is followed for all the specimens.

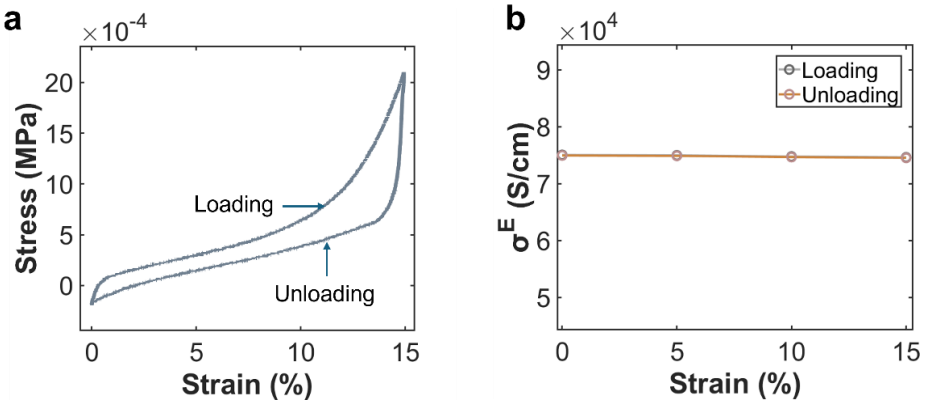

Figure S10. Additional electromechanical behavior of mesh 40 CuLMCs during cyclic loading-unloading test. (a) The stress-strain curve shows a hysteresis effect, possibly induced by the fiber-fiber friction, viscoelastic nature of the Ecoflex 00-30 matrix [15], and perhaps liquid metal oxidation as well. (b) The electrical conductivity curve remained unchanged in a loading-unloading cycle.

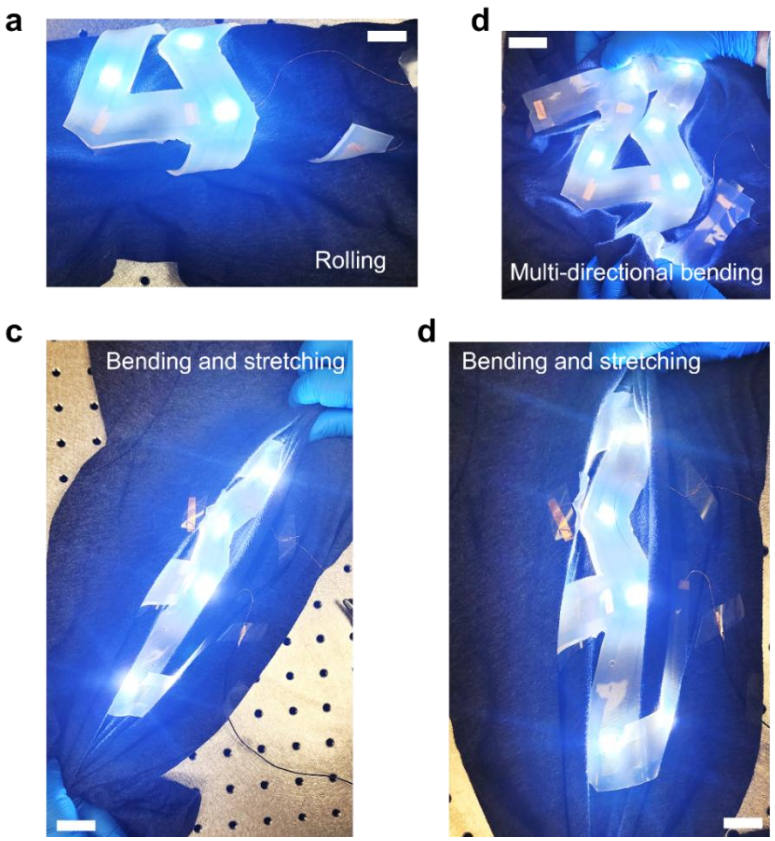

Figure S11. Application of CuLMCs as stretchable and wearable interconnects mounted on textiles under extreme conditions. (a) Rolling. (b) Multi-directional bending. (c-d) Simultaneous bending and stretching from diagonal direction and vertical direction. The luminosity is stable for all cases. Scale bar, 3cm.

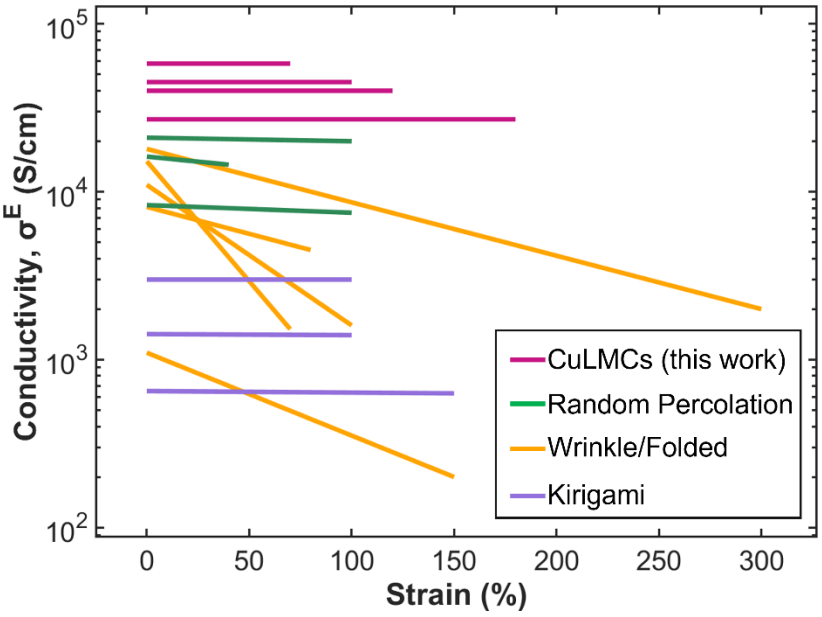

Figure S12. Comparison of the electrical conductivity-strain relations of CuLMCs with random percolation, structure (Kirigami) and geometry-based (wrinkle/folded) composites. The random percolation-based designs (liquid metal and hybrid fillers) exhibit high electrical conductivity and nearly constant conductivity under stretching. The structure-based design with wrinkles, folding, prestrain show mostly strain sensitive behavior. The geometric based design (Kirigami/Origami) exhibits completely flat trends. The CuLMCs display perfectly strain-insensitive behavior as well as high electrical conductivity. Detailed data are tabulated in Table S6.

Table S5. Electrical resistance of CuCs and CuLMCs fabricated from different mesh sizes.

Mesh Size	CuC [Ω]	CuLMC [Ω]
20	1.03	0.0029
30	0.62	0.0033
40	1.68	0.0036
60	1.31	0.0048

Table S6. Survey of electrical conductivity of random percolation, structure, and geometry-based stretchable conductive composites.

Material	Design Mechanism	Initial Electrical Conductivity [S/cm]	Maximum Strain [%]	Electrical Conductivity at Maximum Strain [S/cm]	Ref.
CuLMCs:					
Mesh 20 CuLMC (-50% prestrain)	prestrain	27000	180	27000	This work
Mesh 30 CuLMC (-35% prestrain)	prestrain	40000	120	40000	This work
Mesh 40 CuLMC (-33% prestrain)	prestrain	45000	100	44000	This work
Mesh 60 CuLMC (-26% prestrain)	prestrain	58000	70	58000	This work
Random Percolation Based:					
GaInSn PDMS	percolation	16200	40	14500	[1]
LMP PU	percolation	21000	100	20000	[3]
Ag flakes EGaInPs	percolation	8331	100	7500	[16]
Prestrain/wrinkle/folded Based [a)]:					
Ag SRAR	prestrain	1100	150	200	[17]
AuNP PDMS	wrinkle	11000	100	1600	[18]
Ni PDMS	wrinkle	15200	70	1520	[19]
EGaIn SBS	wrinkle	18000	300	2000	[20]
AgNW PDMS	wrinkle	8130	80	4500	[6]
Origami/Kirigami Based Design [b)]:					
LM Paper	Kirigami	3000	100	3000	[21]
Ag NF (below 100^0C)	Kirigami	1420	100	1400	[22]
PEDOT Fe_2O_3	Kirigami	650	150	630	[23]

[a)]2D based and thin films-based designs are avoided; [b)]Kirigami and origami are presented only for the comparison.

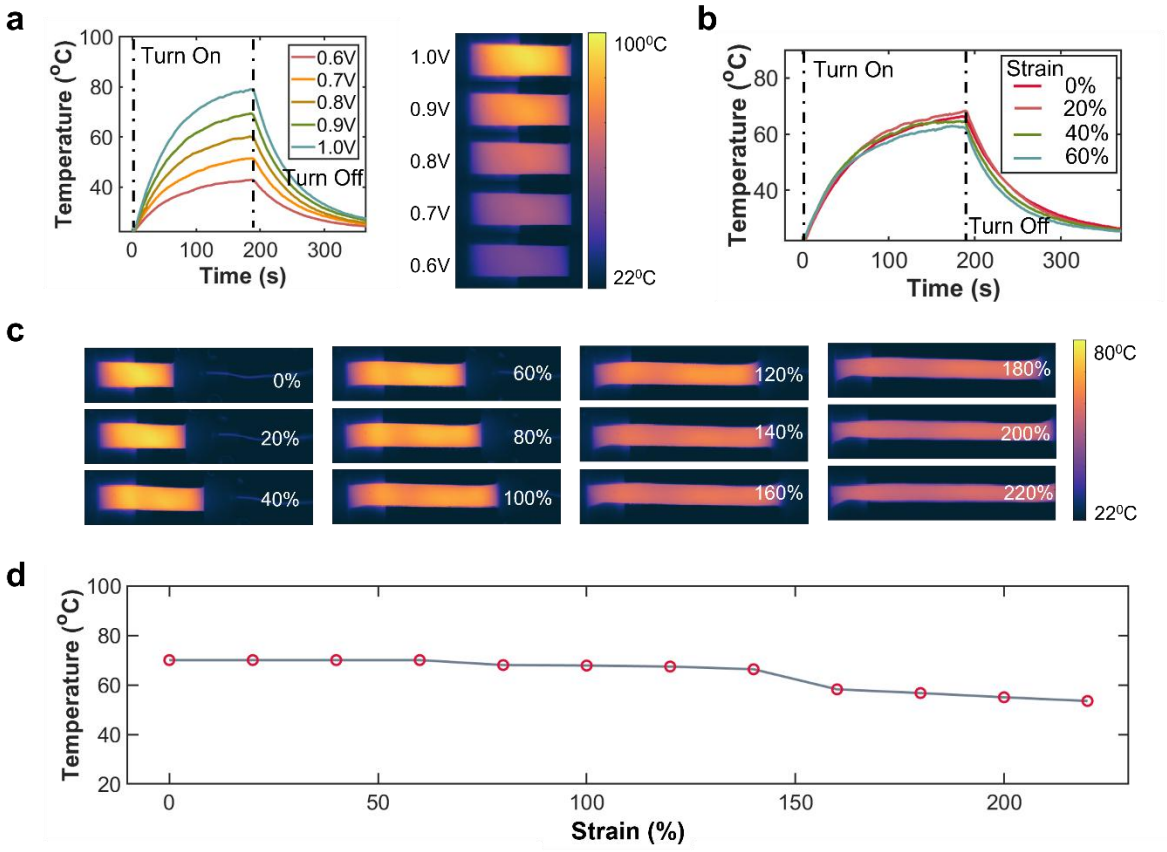

Figure S13. Joule heating behavior of prestrained (angled mesh) brass-LM composite under mechanical stretching. To attain higher stretchability, the brass-LM mesh 30 was prestrained to -60%. The conductivity for the prestrained brass-LM composite is 4838S/cm before stretching. (a) Temperature profile vs time under various voltages (0.6 to 1.0V) for unstretched samples. (b) Temperature evolution under various strain levels. (c) The thermal images of a composite heater under stretching from 0 to 220% strain. (d) The average surface temperature of the Joule heater under stretching. The Joule heating behavior is nearly strain-insensitive up to 140% of strain.

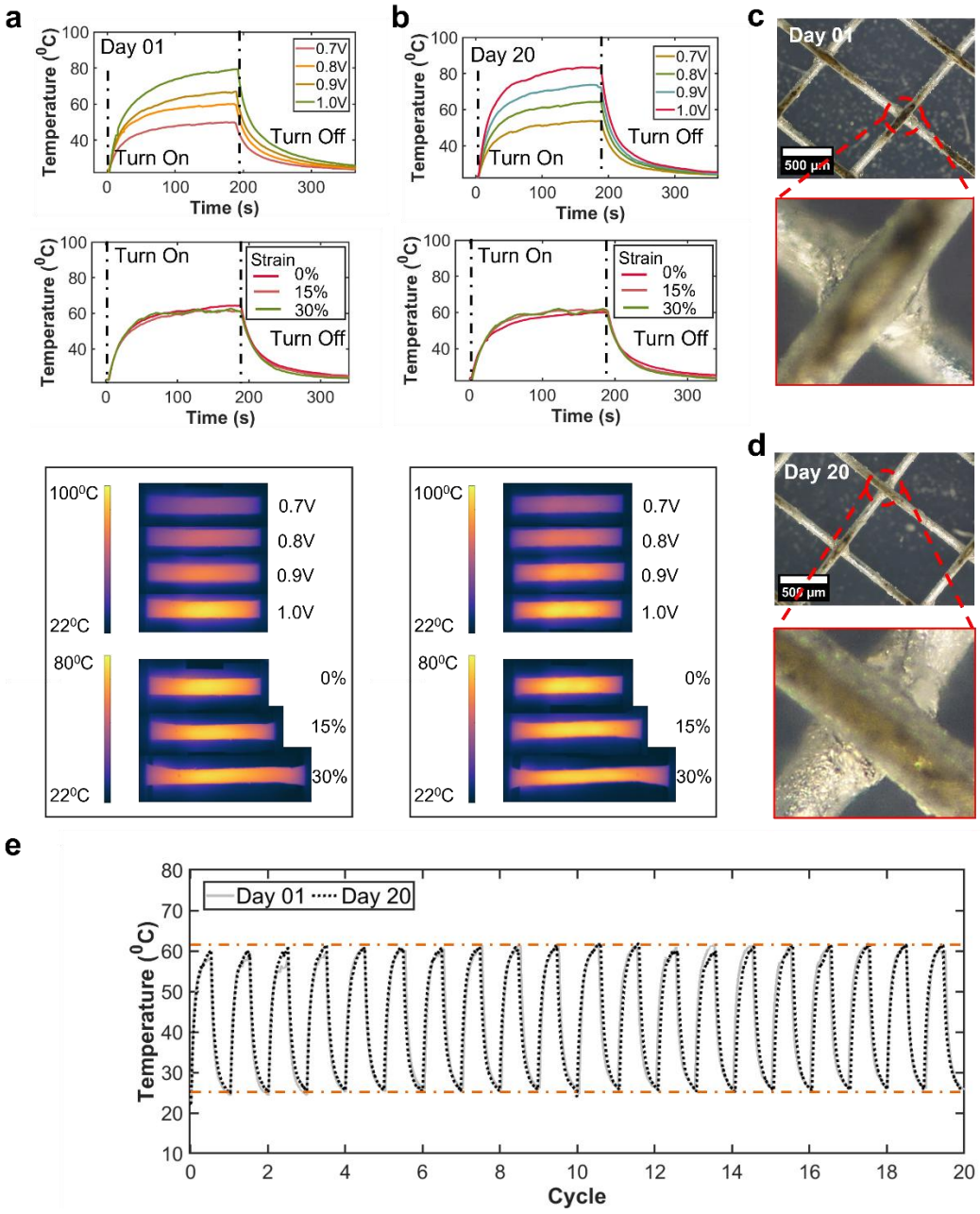

Figure S14. Joule heating stability analysis of brass-LM composites on day 1 and day 20. (a) The heating and cooling curves with voltage 0.7 to 1.0V (top) on day 1. Temperature evolution under different strain levels (middle). Thermal images of both original state and stretched condition (bottom). (b) The top graph depicts the heating and cooling curves for the day 20 sample from 0.7 to 1.0 V. The middle section shows the temperature response of the stretched sample during the heating and cooling process. The bottom row presents thermal images of both original state and stretched condition (bottom). (c-d) Optical microscopy images of the heater on day 1 and day 20. The images confirm the presence of fluidic LM in the junction while showing no observable signs of corrosion in both cases. (e) Cyclic heating behavior under an applied voltage of 0.8V. Temperature-cycle trends depict heater response on day 1 and day 20, indicating a consistent thermal profile over 20 cycles.

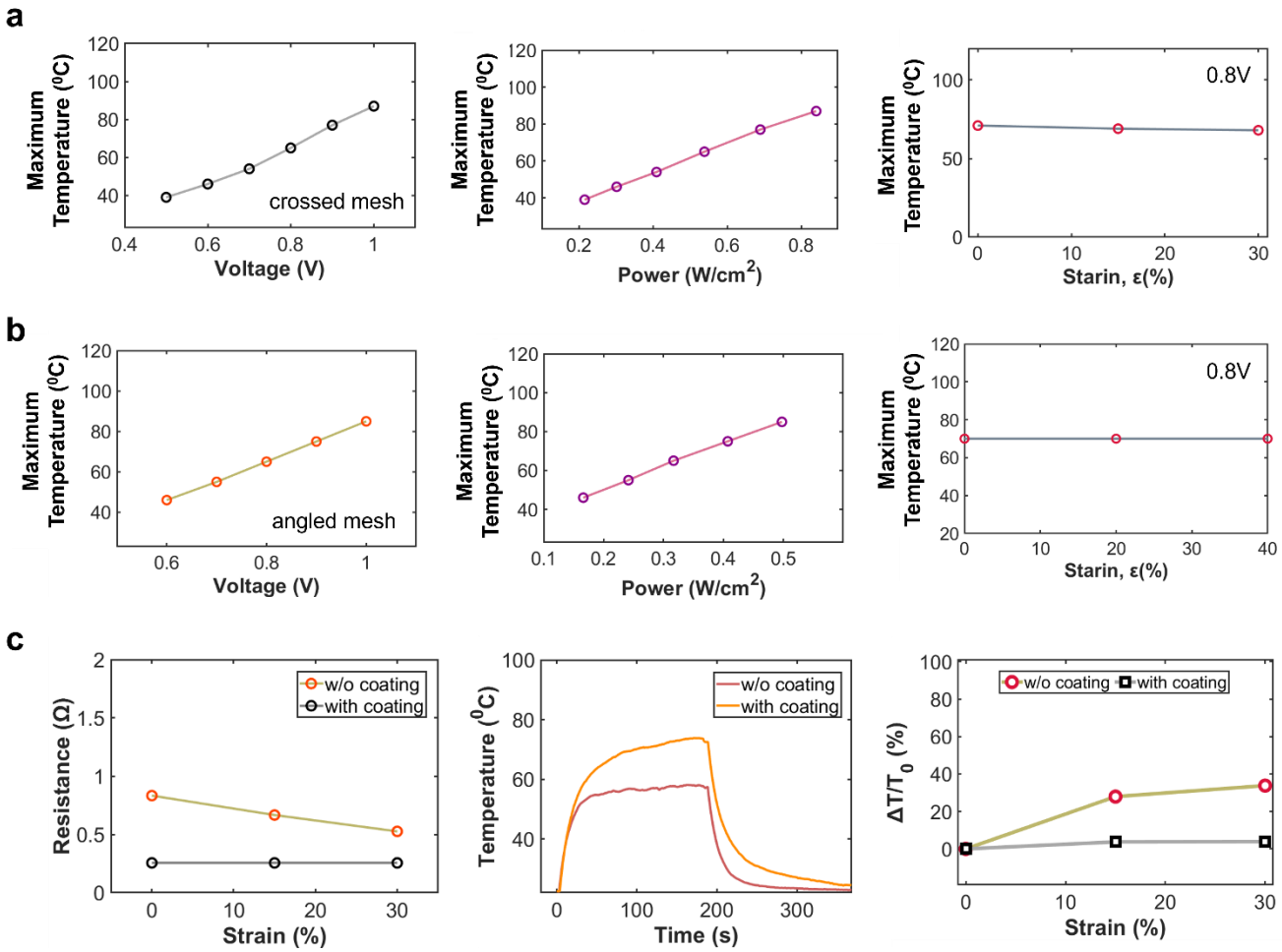

Figure S15. Joule heating performance of the crossed mesh and angled mesh (prestrained) brass-LM composite heaters. (a) The relationship of maximum temperature with voltage, power consumption, and strain of the crossed mesh brass-LM heater. (b) The relationship of maximum temperature with voltage, power consumption, and strain of the angled mesh brass-LM heater. (c) Effect of LM junctions on the Joule heating performance of the crossed mesh brass-LM composites. Adding LM junctions significantly improves the strain-insensitivity and elevates the temperature profile higher.

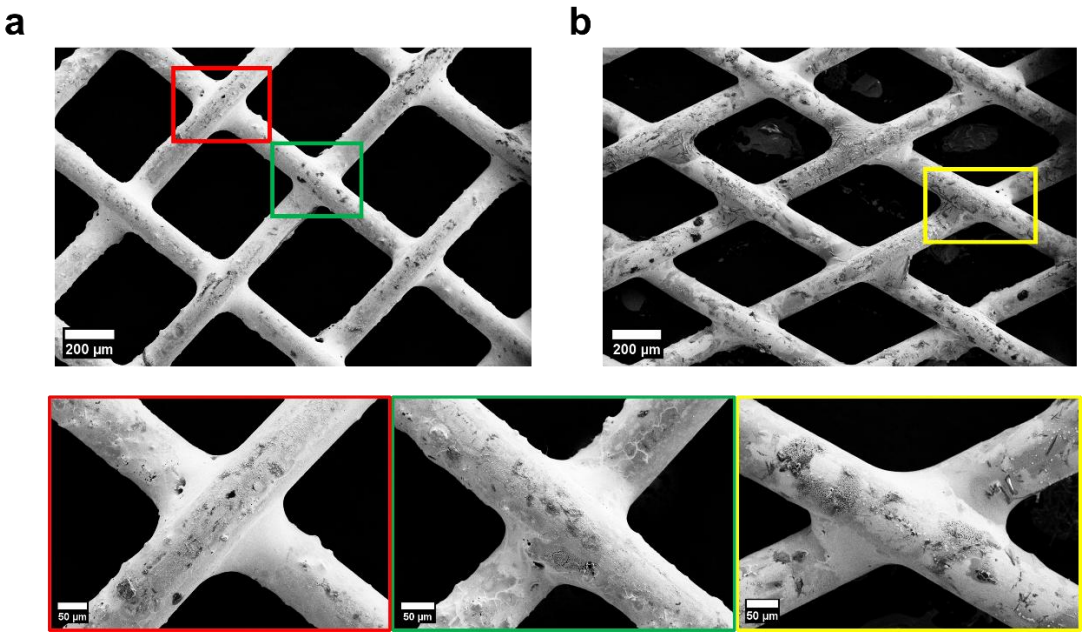

Figure S16. SEM images of conductive LM junction. (a) Junctions in a crossed mesh. (b) Junctions in an angled mesh.

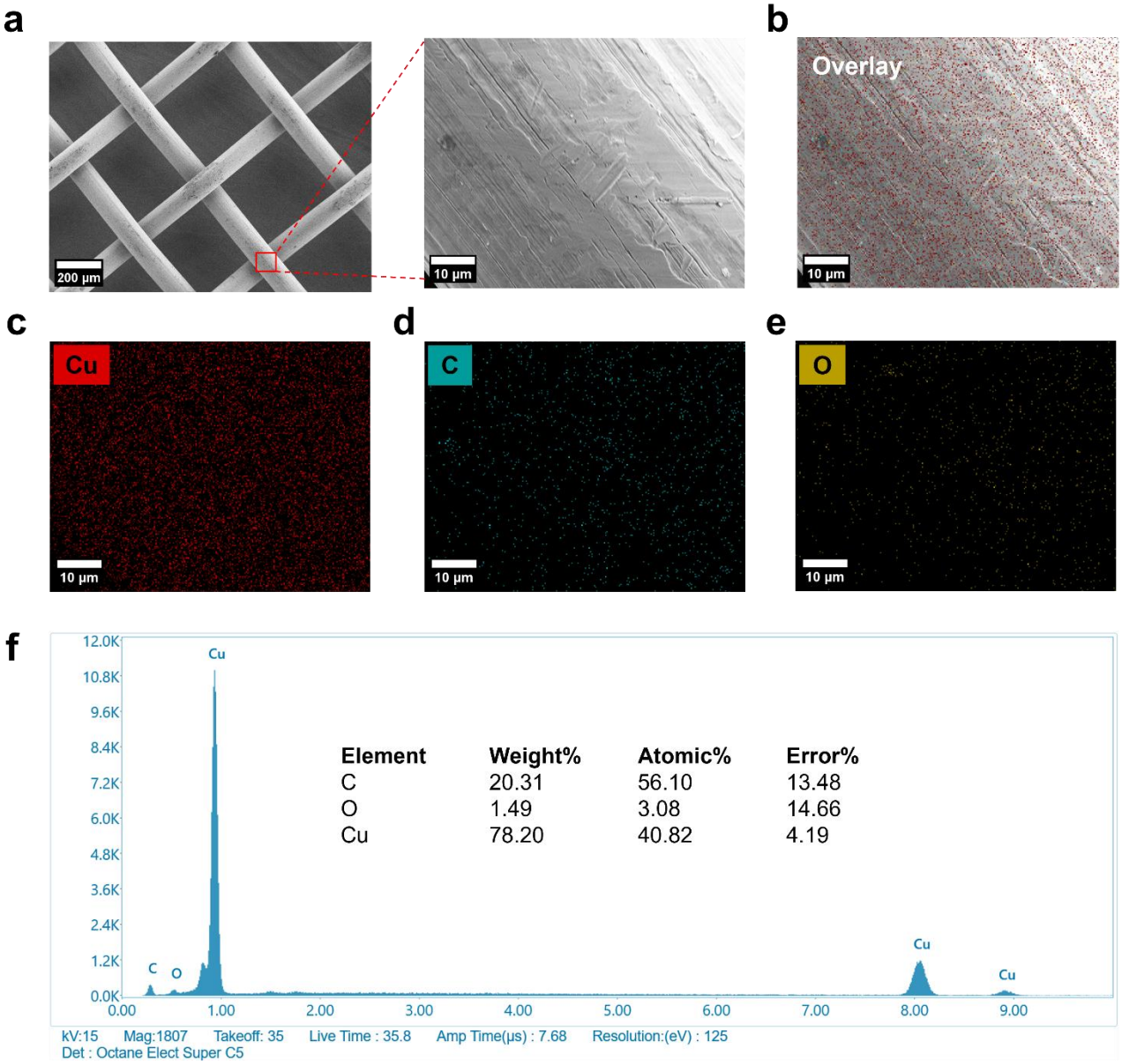

Figure S17. EDS mapping of carbon coated copper mesh. **(**a) SEM images of carbon coated copper mesh. EDS element map of (b) all elements, (c) copper, (d) carbon, and (e) oxygen. (f) EDS spectra of Cu-C and respective element.

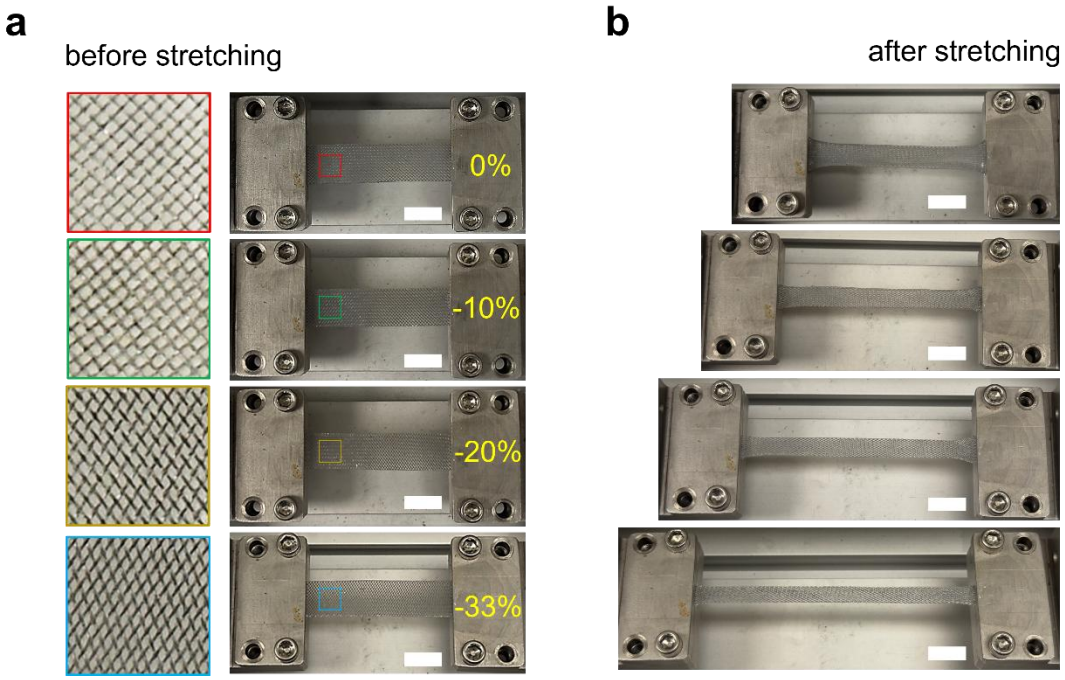

Figure S18. Additional optical images of 0%, -10%, -20%, and -33 prestrained mesh 40 CuLMC (a) before, and (b) after stretching during electromechanical testing. Scale bar is 10mm.

Table S7. Survey of soft and stretchable composites for Joule heating applications.

Material	Structure	Stretchability [%]	Temperature at 0% Strain [°C]	Temperature at maximum Strain [°C]	Temperature Variation, ΔT/T [%]	Ref.
Brass-LM/PDMS	Composites	30	72	69.5	3.5	This work
Brass-LM/PDMS	Composites	140	70	66	5.7	This work
NW/PDMS	Composites	30	80	40	50	[24]
AgNF/SF	Composites	75	45	38	15.6	[25]
CuZr/PDMS	Composites	70	120	90	25	[26]
CNT/TRH	Composites /Textiles	100	100	78	22	[27]
CMT/PDMS	Composites /Textiles	70	120	140	16.7	[28]
GNS/SBR	Composites	70	165	150	9.1	[29]
EGaIn/PDMS	Composites	75	100	90	10	[30]
LM/CIP/PDMS	Composites	50	42	45	7.1	[31]
AgNW/SBS	Composites	50	44	38	13.6	[32]
CuNW/PE	Fibers/Textiles	80	68	50	26.5	[33]
CNT/PDMS	Composites	30	155	140	9.7	[34]
EGaIn/Ag/SEBS	Composites	120	48	40	16.7	[35]

References:

(1) Liang, S.; Li, Y.; Chen, Y.; Yang, J.; Zhu, T.; Zhu, D.; He, C.; Liu, Y.; Handschuh-Wang, S.; Zhou, X. Liquid Metal Sponges for Mechanically Durable, All-Soft, Electrical Conductors. *J. Mater. Chem. C* **2017**, *5* (7), 1586–1590. https://doi.org/10.1039/C6TC05358K.

(2) Markvicka, E. J.; Bartlett, M. D.; Huang, X.; Majidi, C. An Autonomously Electrically Self-Healing Liquid Metal–Elastomer Composite for Robust Soft-Matter Robotics and Electronics. *Nat. Mater.* **2018**, *17* (7), 618–624. https://doi.org/10.1038/s41563-018-0084-7.

(3) Lee, W.; Kim, H.; Kang, I.; Park, H.; Jung, J.; Lee, H.; Park, H.; Park, J. S.; Yuk, J. M.; Ryu, S.; Jeong, J.-W.; Kang, J. Universal Assembly of Liquid Metal Particles in Polymers Enables Elastic Printed Circuit Board. *Science* **2022**, *378* (6620), 637–641. https://doi.org/10.1126/science.abo6631.

(4) Yoon, Y.; Samanta, K.; Lee, H.; Lee, K.; Tiwari, A. P.; Lee, J.; Yang, J.; Lee, H. Highly Stretchable and Conductive Silver Nanoparticle Embedded Graphene Flake Electrode Prepared by In Situ Dual Reduction Reaction. *Sci. Rep.* **2015**, *5* (1), 14177. https://doi.org/10.1038/srep14177.

(5) Park, M.; Im, J.; Shin, M.; Min, Y.; Park, J.; Cho, H.; Park, S.; Shim, M.-B.; Jeon, S.; Chung, D.-Y.; Bae, J.; Park, J.; Jeong, U.; Kim, K. Highly Stretchable Electric Circuits from a Composite Material of Silver Nanoparticles and Elastomeric Fibres. *Nat. Nanotechnol.* **2012**, *7* (12), 803–809. https://doi.org/10.1038/nnano.2012.206.

(6) Xu, F.; Zhu, Y. Highly Conductive and Stretchable Silver Nanowire Conductors. *Adv. Mater.* **2012**, *24* (37), 5117–5122. https://doi.org/10.1002/adma.201201886.

(7) Miyamoto, A.; Lee, S.; Cooray, N. F.; Lee, S.; Mori, M.; Matsuhisa, N.; Jin, H.; Yoda, L.; Yokota, T.; Itoh, A.; Sekino, M.; Kawasaki, H.; Ebihara, T.; Amagai, M.; Someya, T. Inflammation-Free, Gas-Permeable, Lightweight, Stretchable on-Skin Electronics with Nanomeshes. *Nat. Nanotechnol.* **2017**, *12* (9), 907–913. https://doi.org/10.1038/nnano.2017.125.

(8) Choi, S.; Han, S. I.; Jung, D.; Hwang, H. J.; Lim, C.; Bae, S.; Park, O. K.; Tschabrunn, C. M.; Lee, M.; Bae, S. Y.; Yu, J. W.; Ryu, J. H.; Lee, S.-W.; Park, K.; Kang, P. M.; Lee, W. B.; Nezafat, R.; Hyeon, T.; Kim, D.-H. Highly Conductive, Stretchable and Biocompatible Ag–Au Core–Sheath Nanowire Composite for Wearable and Implantable Bioelectronics. *Nat. Nanotechnol.* **2018**, *13* (11), 1048–1056. https://doi.org/10.1038/s41565-018-0226-8.

(9) Parida, K.; Thangavel, G.; Cai, G.; Zhou, X.; Park, S.; Xiong, J.; Lee, P. S. Extremely Stretchable and Self-Healing Conductor Based on Thermoplastic Elastomer for All-Three-Dimensional Printed Triboelectric Nanogenerator. *Nat. Commun.* **2019**, *10* (1), 2158. https://doi.org/10.1038/s41467-019-10061-y.

(10) Wang, J.; Cai, G.; Li, S.; Gao, D.; Xiong, J.; Lee, P. S. Printable Superelastic Conductors with Extreme Stretchability and Robust Cycling Endurance Enabled by Liquid-Metal Particles. *Adv. Mater.* **2018**, *30* (16), 1706157. https://doi.org/10.1002/adma.201706157.

(11) Wu, Y.; Deng, Z.; Peng, Z.; Zheng, R.; Liu, S.; Xing, S.; Li, J.; Huang, D.; Liu, L. A Novel Strategy for Preparing Stretchable and Reliable Biphasic Liquid Metal. *Adv. Funct. Mater.* **2019**, *29* (36), 1903840. https://doi.org/10.1002/adfm.201903840.

(12) Zu, W.; Carranza, H. E.; Bartlett, M. D. Enhancing Electrical Conductivity of Stretchable Liquid Metal–Silver Composites through Direct Ink Writing. *ACS Appl. Mater. Interfaces* **2024**, acsami.4c02466. https://doi.org/10.1021/acsami.4c02466.

(13) Shukla, D.; Wang, H.; Awartani, O.; Dickey, M. D.; Zhu, Y. Surface Embedded Metal Nanowire–Liquid Metal–Elastomer Hybrid Composites for Stretchable Electronics. *ACS Appl. Mater. Interfaces* **2024**, *16* (11), 14183–14197. https://doi.org/10.1021/acsami.4c00318.

(14) Park, S.; Thangavel, G.; Parida, K.; Li, S.; Lee, P. S. A Stretchable and Self-Healing Energy Storage Device Based on Mechanically and Electrically Restorative Liquid-Metal Particles and Carboxylated Polyurethane Composites. *Adv. Mater.* **2019**, *31* (1), 1805536. https://doi.org/10.1002/adma.201805536.
(15) Liao, Z.; Hossain, M.; Yao, X.; Navaratne, R.; Chagnon, G. A Comprehensive Thermo-Viscoelastic Experimental Investigation of Ecoflex Polymer. *Polym. Test.* **2020**, *86*, 106478. https://doi.org/10.1016/j.polymertesting.2020.106478.
(16) Yang, Y.; Liu, J.; Chen, G.; Gao, A.; Wang, J.; Wang, J. Stretchable Fibers with Highly Conductive Surfaces and Robust Electromechanical Performances for Electronic Textiles. *ACS Appl. Mater. Interfaces* **2024**, *16* (5), 6122–6132. https://doi.org/10.1021/acsami.3c16819.
(17) Won, J.; Mondal, S.; Park, J.; Wang, W.; Lee, H.; Kim, S.; Shin, B.; Sathi, S. G.; Nah, C. Highly Stretchable Wrinkled Electrode Based on Silver Ink-Elastomer Nanocomposite with Excellent Fatigue Resistance. *Polym. Compos.* **2020**, *41* (6), 2210–2223. https://doi.org/10.1002/pc.25532.
(18) Lee, S.; Song, Y.; Ko, Y.; Ko, Y.; Ko, J.; Kwon, C. H.; Huh, J.; Kim, S.-W.; Yeom, B.; Cho, J. A Metal-Like Conductive Elastomer with a Hierarchical Wrinkled Structure. *Adv. Mater.* **2020**, *32* (7), 1906460. https://doi.org/10.1002/adma.201906460.
(19) Yoo, C.; Lee, S.; Song, Y.; Chang, W.; Park, M. K.; Ko, Y.; Cho, J. Micro/Nano-Wrinkled Elastomeric Electrodes Enabling High Energy Storage Performance and Various Form Factors. *Carbon Energy* **2023**, *5* (12), e335. https://doi.org/10.1002/cey2.335.
(20) Ma, Z.; Huang, Q.; Xu, Q.; Zhuang, Q.; Zhao, X.; Yang, Y.; Qiu, H.; Yang, Z.; Wang, C.; Chai, Y.; Zheng, Z. Permeable Superelastic Liquid-Metal Fibre Mat Enables Biocompatible and Monolithic Stretchable Electronics. *Nat. Mater.* **2021**, *20* (6), 859–868. https://doi.org/10.1038/s41563-020-00902-3.
(21) Li, X.; Zhu, P.; Zhang, S.; Wang, X.; Luo, X.; Leng, Z.; Zhou, H.; Pan, Z.; Mao, Y. A Self-Supporting, Conductor-Exposing, Stretchable, Ultrathin, and Recyclable Kirigami-Structured Liquid Metal Paper for Multifunctional E-Skin. *ACS Nano* **2022**, *16* (4), 5909–5919. https://doi.org/10.1021/acsnano.1c11096.
(22) Lyu, J.; Hammig, M. D.; Liu, L.; Xu, L.; Chi, H.; Uher, C.; Li, T.; Kotov, N. A. Stretchable Conductors by Kirigami Patterning of Aramid-Silver Nanocomposites with Zero Conductance Gradient. *Appl. Phys. Lett.* **2017**, *111* (16), 161901. https://doi.org/10.1063/1.5001094.
(23) Diao, Y.; Woon, R.; Yang, H.; Chow, A.; Wang, H.; Lu, Y.; D'Arcy, J. M. Kirigami Electrodes of Conducting Polymer Nanofibers for Wearable Humidity Dosimeters and Stretchable Supercapacitors. *J. Mater. Chem. A* **2021**, *9* (15), 9849–9857. https://doi.org/10.1039/D0TA11335B.
(24) Hong, S.; Lee, H.; Lee, J.; Kwon, J.; Han, S.; Suh, Y. D.; Cho, H.; Shin, J.; Yeo, J.; Ko, S. H. Highly Stretchable and Transparent Metal Nanowire Heater for Wearable Electronics Applications. *Adv. Mater.* **2015**, *27* (32), 4744–4751. https://doi.org/10.1002/adma.201500917.
(25) Huang, J.; Xu, Z.; Qiu, W.; Chen, F.; Meng, Z.; Hou, C.; Guo, W.; Liu, X. Y. Stretchable and Heat-Resistant Protein-Based Electronic Skin for Human Thermoregulation. *Adv. Funct. Mater.* **2020**, *30* (13), 1910547. https://doi.org/10.1002/adfm.201910547.
(26) An, B. W.; Gwak, E.-J.; Kim, K.; Kim, Y.-C.; Jang, J.; Kim, J.-Y.; Park, J.-U. Stretchable, Transparent Electrodes as Wearable Heaters Using Nanotrough Networks of Metallic Glasses with Superior Mechanical Properties and Thermal Stability. *Nano Lett.* **2016**, *16* (1), 471–478. https://doi.org/10.1021/acs.nanolett.5b04134.
(27) Li, Y.; Zhang, Z.; Li, X.; Zhang, J.; Lou, H.; Shi, X.; Cheng, X.; Peng, H. A Smart, Stretchable Resistive Heater Textile. *J. Mater. Chem. C* **2017**, *5* (1), 41–46. https://doi.org/10.1039/C6TC04399B.

(28) Zhang, M.; Wang, C.; Liang, X.; Yin, Z.; Xia, K.; Wang, H.; Jian, M.; Zhang, Y. Weft-Knitted Fabric for a Highly Stretchable and Low-Voltage Wearable Heater. *Adv. Electron. Mater.* **2017**, *3* (9), 1700193. https://doi.org/10.1002/aelm.201700193.
(29) Wang, F.; Wang, W.; Mu, X.; Mao, J. Anisotropic Conductive, Tough and Stretchable Heater Based on Nacre-like Crumpled Graphene Composite. *Chem. Eng. J.* **2020**, *395*, 125183. https://doi.org/10.1016/j.cej.2020.125183.
(30) Wang, G.; Chen, J.; Zheng, W.; Shen, B. High-Efficiency Flexible Liquid Metal/Elastomer Composite Film with Designability for Strain-Invariant Electromagnetic Shielding and Joule-Heating Applications. *Chem. Eng. J.* **2024**, *488*, 151052. https://doi.org/10.1016/j.cej.2024.151052.
(31) Kim, S.; Saito, M.; Wei, Y.; Bhuyan, P.; Choe, M.; Fujie, T.; Mondal, K.; Park, S. Stretchable and Wearable Polymeric Heaters and Strain Sensors Fabricated Using Liquid Metals. *Sens. Actuators Phys.* **2023**, *355*, 114317. https://doi.org/10.1016/j.sna.2023.114317.
(32) Choi, S.; Park, J.; Hyun, W.; Kim, J.; Kim, J.; Lee, Y. B.; Song, C.; Hwang, H. J.; Kim, J. H.; Hyeon, T.; Kim, D.-H. Stretchable Heater Using Ligand-Exchanged Silver Nanowire Nanocomposite for Wearable Articular Thermotherapy. *ACS Nano* **2015**, *9* (6), 6626–6633. https://doi.org/10.1021/acsnano.5b02790.
(33) Cheng, Y.; Zhang, H.; Wang, R.; Wang, X.; Zhai, H.; Wang, T.; Jin, Q.; Sun, J. Highly Stretchable and Conductive Copper Nanowire Based Fibers with Hierarchical Structure for Wearable Heaters. *ACS Appl. Mater. Interfaces* **2016**, *8* (48), 32925–32933. https://doi.org/10.1021/acsami.6b09293.
(34) Xu, F.; Aouraghe, M. A.; Xie, X.; Zheng, L.; Zhang, K.; Fu, K. K. Highly Stretchable, Fast Thermal Response Carbon Nanotube Composite Heater. *Compos. Part Appl. Sci. Manuf.* **2021**, *147*, 106471. https://doi.org/10.1016/j.compositesa.2021.106471.
(35) Dong, J.; Tang, X.; Peng, Y.; Fan, C.; Li, L.; Zhang, C.; Lai, F.; He, G.; Ma, P.; Wang, Z.; Wei, Q.; Yan, X.-P.; Qian, H.-L.; Huang, Y.; Liu, T. Highly Permeable and Ultrastretchable E-Textiles with EGaIn-Superlyophilicity for on-Skin Health Monitoring, Joule Heating, and Electromagnetic Shielding. *Nano Energy* **2023**, *108*, 108194. https://doi.org/10.1016/j.nanoen.2023.108194.